CANCER

Multivalent state transitions shape the intratumoral composition of small cell lung carcinoma

Priyanka Gopal[1], Aaron Petty[2], Kevin Rogacki[1], Titas Bera[1], Rohan Bareja[3], Craig D. Peacock[4]†, Mohamed E. Abazeed[1,5]*

Copyright © 2022 The Authors, some rights reserved; exclusive licensee American Association for the Advancement of Science. No claim to original U.S. Government Works. Distributed under a Creative Commons Attribution NonCommercial License 4.0 (CC BY-NC).

Studies to date have not resolved how diverse transcriptional programs contribute to the intratumoral heterogeneity of small cell lung carcinoma (SCLC), an aggressive tumor associated with a dismal prognosis. Here, we identify distinct and commutable transcriptional states that confer discrete functional attributes in individual SCLC tumors. We combine an integrative approach comprising the transcriptomes of 52,975 single cells, high-resolution measurement of cell state dynamics at the single-cell level, and functional and correlative studies using treatment naïve xenografts with associated clinical outcomes. We show that individual SCLC tumors contain distinctive proportions of stable cellular states that are governed by bidirectional cell state transitions. Using drugs that target the epigenome, we reconfigure tumor state composition in part by altering individual state transition rates. Our results reveal new insights into how single-cell transition behaviors promote cell state equilibrium in SCLC and suggest that facile plasticity underlies its resistance to therapy and lethality.

INTRODUCTION

The use of nongenetic means to diversify phenotypes provides organisms with the ability to adapt quickly to environmental changes (*1*). This diversity can promote survival, especially in the context of extreme environmental shifts (*2*). Similarly, cancers maintain stable proportions of cells in several distinct transcriptionally defined states categorized on the basis of developmental programs (e.g., "stem"-like, epithelial, mesenchymal, neural, and neuroendocrine) or additional undefined gene expression states (*3*, *4*). Within individual tumors, cell state transitions could be modulated by environmental cues, cell-cell signaling, and/or stochastic switches in gene expression programs (*5*), with the potential to skew state proportions, at least transiently. Critically, anticancer therapies appear to preferentially kill specific cancer cell states, resulting in predictable changes in phenotypic proportions (*4*, *6*, *7*). Despite some preliminary observations regarding cell-cell switches and state equilibrium in some cancers, very little is known about the regulation of the proportions of cancer cells in the various cell states, the types and rates of transitions across and within cancer types, and if multistate tumors can be modulated to enhance the prospect of a tumor's extinction (*8*).

Small cell lung carcinoma (SCLC) is an aggressive disease that accounts for ~15% of all lung cancers and affects ~200,000 patients annually worldwide (*9*). A diagnosis of SCLC is typically associated with a dismal prognosis, with most patients succumbing within 1 year and a 5-year survival rate of only 6%. First-line treatments include the combination of cisplatin and etoposide alone or with radiotherapy (*10*). Although most patients respond to first-line therapy, most patients also experience disease recurrence. In contrast to other types of lung cancer, there have been no major advances in the use of targeted therapies, and the benefits of immunotherapy have been modest (*11*–*13*). New paradigms and approaches focused on advancing therapeutic strategies in patients with SCLC are urgently needed.

Large-scale sequencing of SCLC has not revealed consistent cooccurrence or mutual exclusivity of genetic alterations, frustrating efforts to stratify patients on the basis of the genome (*14*). On the other hand, there are indications of transcriptionally distinct subtypes of SCLC (*15*–*20*). These studies have indicated at least three transcriptional clusters, with the largest representing an *ASCL1*^{high} *NEUROD1*^{low} subtype, the second largest representing a *NEUROD1*^{high} subtype, and a small number of tumors expressing low levels of both *ASCL1* and *NEUROD1*, but high levels of *YAP1*. *ASCL1* is a basic helix-loop-helix (bHLH) transcription factor (TF) that is a marker of neuroendocrine differentiation (*21*). *NEUROD1* is also a bHLH TF that is required for neural development (*18*). *YAP1*, a regulator of transcription that is inhibited by the Hippo growth signaling pathway, is expressed in mesenchymal cells but is undetectable or low in most SCLC cell lines (*22*). A fourth TF, *POU2F3*, was recently identified as defining a previously unappreciated tuft cell variant of SCLC (*23*). Despite a proposed quaternary taxonomy (*16*, *24*), some immunohistochemical (IHC) analyses have not confirmed a Yap1 subtype (*25*). Therefore, SCLC transcriptional classification remains, at least in part, discordant and incomplete.

Further confounding the attempts to stratify SCLC tumors into discrete categories are suggestions of intratumoral heterogeneity. Morphologically different cell types have been noted in a number of SCLC cell lines, including some with mixtures of cells in suspension in combination with variably adherent monolayers (*26*). Expression profiling of these distinct populations suggests that the suspended cells are more likely to have neuroendocrine features, whereas the adherent population adopts a less neuroendocrine,

[1]Department of Radiation Oncology, Northwestern University, Feinberg School of Medicine, 251 E. Huron St., Galter Pavilion LC-178, Chicago, IL 60611, USA. [2]Department of Translational Hematology Oncology Research, Cleveland Clinic, 2111 East 96th St./NE-6, Cleveland, OH 44195, USA. [3]Institute for Computational Biomedicine, Weill Cornell Medicine, 1305 York Ave., New York, NY 10021, USA. [4]Department of Genetics and Genome Sciences, Case Western Reserve University, 2109 Adelbert Road, Biomedical Research Building 647B, Cleveland, OH 44106, USA. [5]Robert H. Lurie Cancer Center, Northwestern University, 303 E. Superior St./Lurie 7, Chicago, IL 60611, USA.
†Present address: Department of Medicine, Case Western Reserve University, 2103 Cornell Rd., WRB 3-301, Cleveland, OH 44106, USA.
*Corresponding author. Email: mabazeed@northwestern.edu

more mesenchymal expression profile. Mesenchymal cells, expressing *VIM*, *CD44*, and *YAP1* have a reduced proliferative rate, relatively greater chemoresistance, and support the survival, growth, and migration of the neuroendocrine subtype of cells within admixed tumors (*27*, *28*). Additional data support a role for Notch signaling, generally suppressed in the predominant *ASCL1*^{high} subtype, in inducing a neuroendocrine to mesenchymal fate switch in both mouse and human SCLC cells (*29*–*31*). Studies conducted in genetically engineered mouse models of SCLC and driven by heterologous MYC^{T58A} demonstrate a unidirectional transition from one cell fate (*ASCL1*) to another (*YAP1*), resulting in ultimately homogeneous populations of cell types (*32*, *33*). Recent work using circulating tumor cell–derived xenografts suggests increased intratumoral heterogeneity following treatment resistance, attributed to subtype switching, in human SCLC (*34*, *35*). Overall, these results, combined with a recent single-cell atlas of 21 SCLC tumors, provide indications that distinct cell types can exist within the same SCLC tumor. However, the extent of this heterogeneity in treatment naïve tumors (i.e., not induced by therapeutic stress), the direct observation of subtype switching, the frequency and single-cell kinetics of state transitions, the functional specialization of additional subpopulations, and the impact of tumor state proportions on clinical outcomes have yet to be thoroughly examined. Here, we characterize the proportions and single-cell dynamics of distinct intratumoral subpopulations in SCLC and use epigenetic modifiers to reconfigure tumor composition, with the aim of advancing new therapeutic strategies to improve clinical outcomes.

RESULTS

Distinct gene coexpression networks and the taxonomy of SCLC cell lines

To find categories of SCLC in established cell lines, we performed *k*-means clustering using gene expression data from 53 SCLC cell lines. Four groups were robust to sampling variability (Fig. 1A and fig. S1). We identified differentially expressed genes and gene sets in each group (data S1 and S2). Consistent with the previous identification of some SCLC subtypes (*15*, *36*, *37*), we found differential expression of fate-determining TFs (Fig. 1B). Namely, *ASCL1*, *ISL1*, *NEUROD1*, *INSM1*, and *YAP1* either individually or in aggregate differentially marked each cluster. We selected representative cell lines based on silhouette scores from each group and assessed the concordance between transcript levels and protein levels (Fig. 1C). We found that protein expression was generally associated with gene transcript levels across the representative cell lines.

We posited that gene modules within groups conferred distinct phenotypic traits and morphologies. First, we assessed the proportion of samples within cluster that adhered to the plate. The vast majority of cell lines contained cells that were either adherent or in suspension, with only a few (mainly in cluster II) retaining biphasic growth capacity. Cluster III cells were significantly more likely to grow in suspension compared to cluster I or IV (Fig. 1D). Light microscopy of representative cell lines showed distinct morphology and growth patterns (Fig. 1E). We examined invasion into Matrigel of the same representative cell lines and showed that DMS114 (cluster IV) and, to a lesser extent, H446 (cluster II) had the capacity to invade a complex extracellular environment (Fig. 1F). These results suggested that cell lines were distinct not only in transcriptional states but also in morphology and functional roles (i.e., invasion).

We combined the cellular morphologies and phenotypes of the cell lines with the ontology of differentially expressed genes (individual cluster versus all others) to identify four group-defining characteristics: (i) loosely adherent neuroepithelial cells, (ii) semi-adherent groups of cells with neural-like projections, (iii) suspended, neuroendocrine hormone-producing cells, and (iv) tightly adherent mesenchymal cells that had the capacity to invade matrix and required enzymatic digestion to effect dissociation. Network analyses revealed hubs organized by cell fate–defining TFs, edges that linked dissonant gene expression hubs (i.e., mutually exclusive), and an overall topology that suggested coordinated activity of conserved ontogenetic programs (Fig. 1G and fig. S2). Each network represents the top 100 ranked gene that differentially represent the indicated cluster versus all others. The correlation (linear association) and mutual information (nonlinear measure of association) is between the gene coexpression values within the top genes. Linking the diversity within SCLC with non–small cell lung cancer (NSCLC), some of the genes represented in the mesenchymal cluster were more likely to be expressed by NSCLC cells, suggesting the presence of SCLC groups/states that more closely approximate NSCLC (fig. S3). Therefore, SCLC cell lines cultured in vitro significantly diverged on the basis of distinct gene network activity, appeared to be regulated by individual TF expression, and contained distinct morphologies and phenotypes.

Intratumoral heterogeneity in human SCLC

We collected multiregional fine-needle aspirate biopsies (four to six passes) from patients with SCLC at diagnosis (i.e., treatment naïve) and developed 64 patient-derived xenografts (PDXs). The cancer stage distribution of this cohort closely approximated those found in most clinical practices (Fig. 2A and fig. S4). We performed *k*-means clustering using bulk RNA sequencing (RNA-seq) data from the first passage of the generated PDXs and identified four transcriptional clusters. Nearest centroid correspondence of cell line and PDX-derived clusters showed some associations between clusters across the two cohorts (cell lines versus PDXs) (Fig. 2B). Directed analyses of cluster-defining TFs showed similar patterns in associated groups (Fig. 2C versus Fig. 1B). For example, *ASCL1* levels were highest in PDX clusters I and III (associated with cell line clusters I and III, respectively); *NEUROD1* levels were highest in both cell line and PDX cluster II; PDX cluster I (associated with cell line cluster I) was marked by high *ASCL1* and low *YAP1* expression and, conversely, for cluster IV (associated with cell line cluster IV). Despite these similarities, PDX clusters were more likely to express more than one fate-defining TF in each cluster (Fig. 2C). For example, PDX cluster III expressed moderate to high levels of all fate-defining TFs. Moreover, silhouette width plots, representing the likeness within each cluster, were low across the PDX clusters (fig. S5A). In addition, the variance in the TF gene expression distribution within clusters was significantly higher in PDXs compared to cell lines (fig. S5B). These results suggested that, although retaining some similarities to cell line groups, PDXs were more heterogeneous.

To assess the extent of heterogeneity in individual samples, we first quantified bulk RNA and protein expression (Western blot analysis and IHC) across six representative xenografts (Fig. 2, D and E, and fig. S6). These results indicated that individual tumors

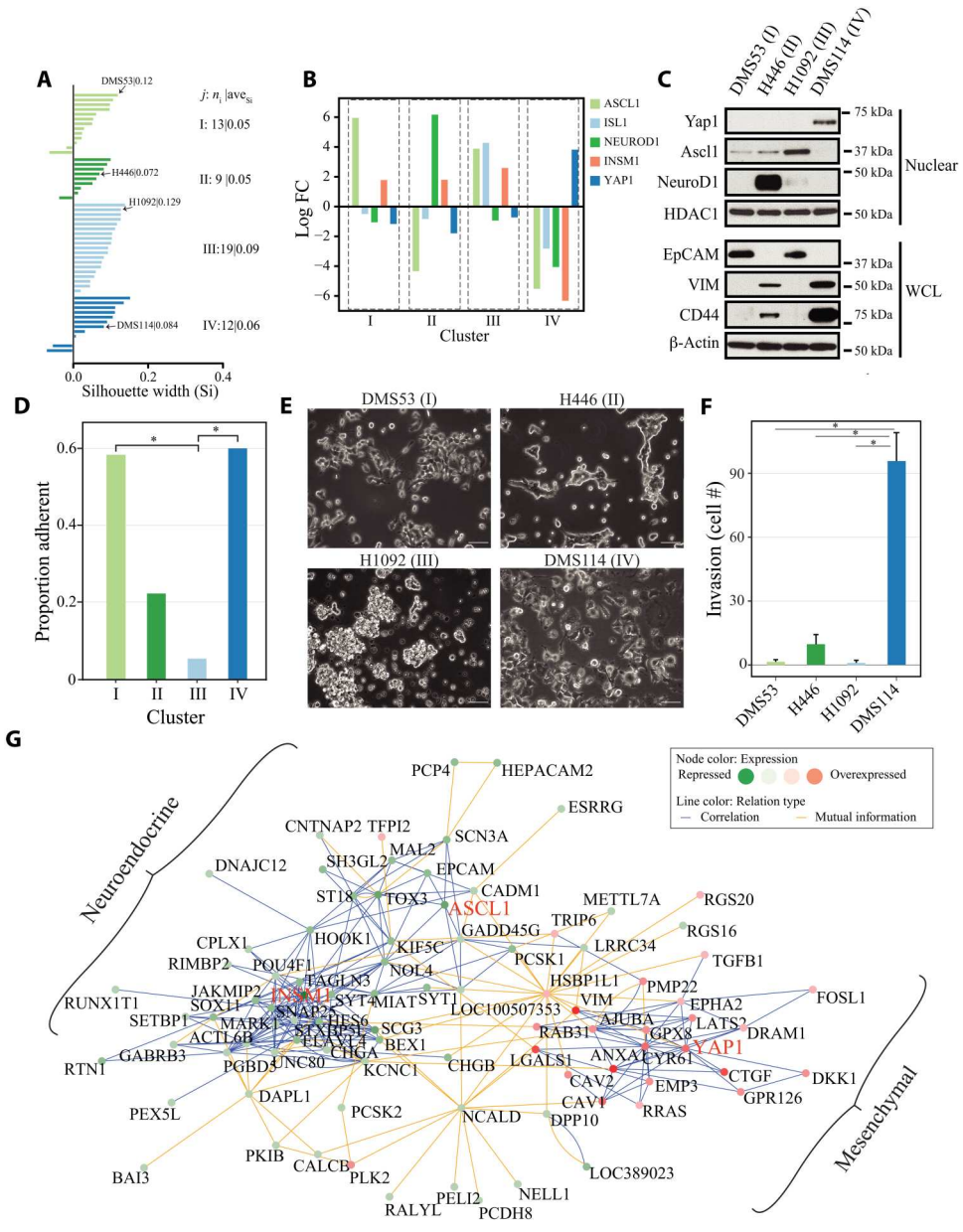

Fig. 1. SCLC cell lines have divergent gene regulatory networks and phenotypes. (**A**) Hierarchical clustering was performed using 53 SCLC cell lines. Silhouette widths, which measure the likeness within each cluster, were calculated. *j*, cluster number; n_i, number of samples in each cluster; ave_{Si}, average silhouette width for each cluster. (**B**) The log fold change (FC) for fate-defining TFs in the indicated cluster versus the rest. (**C**) Representative cell lines, with cluster membership shown in parentheses, were profiled for cluster-defining proteins by immunoblot. WCL, whole cell lysate. (**D**) Proportion of adherent samples for each cluster as annotated by the Cancer Cell Line Encyclopedia (CCLE). Bars represent the means, and the Mann-Whitney test was used for statistical analysis. *$P < 0.05$. (**E**) Phase contrast images (×20) of representative cell lines. (**F**) Cellular invasion using a Boyden chamber assay. Error bars represent SEM of at least three different experiments. The student *t* test with Welch's correction was used for statistical analysis. *$P < 0.05$. (**G**) Gene networks for SCLC cluster IV demonstrate an up-regulation and concomitant down-regulation of mesenchymal and neuroendocrine transcriptional programs, respectively. The networks contain the top 100 ranked genes. Genes are colored on the basis of expression (repressed versus overexpressed), and the intensity of the color represents the extent of expression difference. The edge color indicates the type of coexpression between genes (correlation versus mutual information). *ASCL1*, *INSM1*, and *YAP1* are highlighted by case and color to delineate their positions in the network.

express, by both RNA and protein, one or all the cluster- and fate-defining TFs: *ASCL1*, *NEUROD1*, and *YAP1*. CBX163 represented an exception, an SCLC subtype that lacked neural or neuroendocrine markers and was driven by *POU2F3* (fig. S7). It was retained in our analyses for completeness. To analyze intratumoral heterogeneity at the single-cell level, we generated 52,975 single-cell transcriptomes from the six representative xenografts passaged ex vivo (Fig. 2F). Before single-cell isolation, we determined the proportion of mouse-derived cells by flow cytometry using the murine major histocompatibility complex class I antibody anti–H-2K. Mouse cellular admixture of human ex vivo tumors was very low (0 to 0.1%; fig. S8). We excluded cells and genes with low coverage,

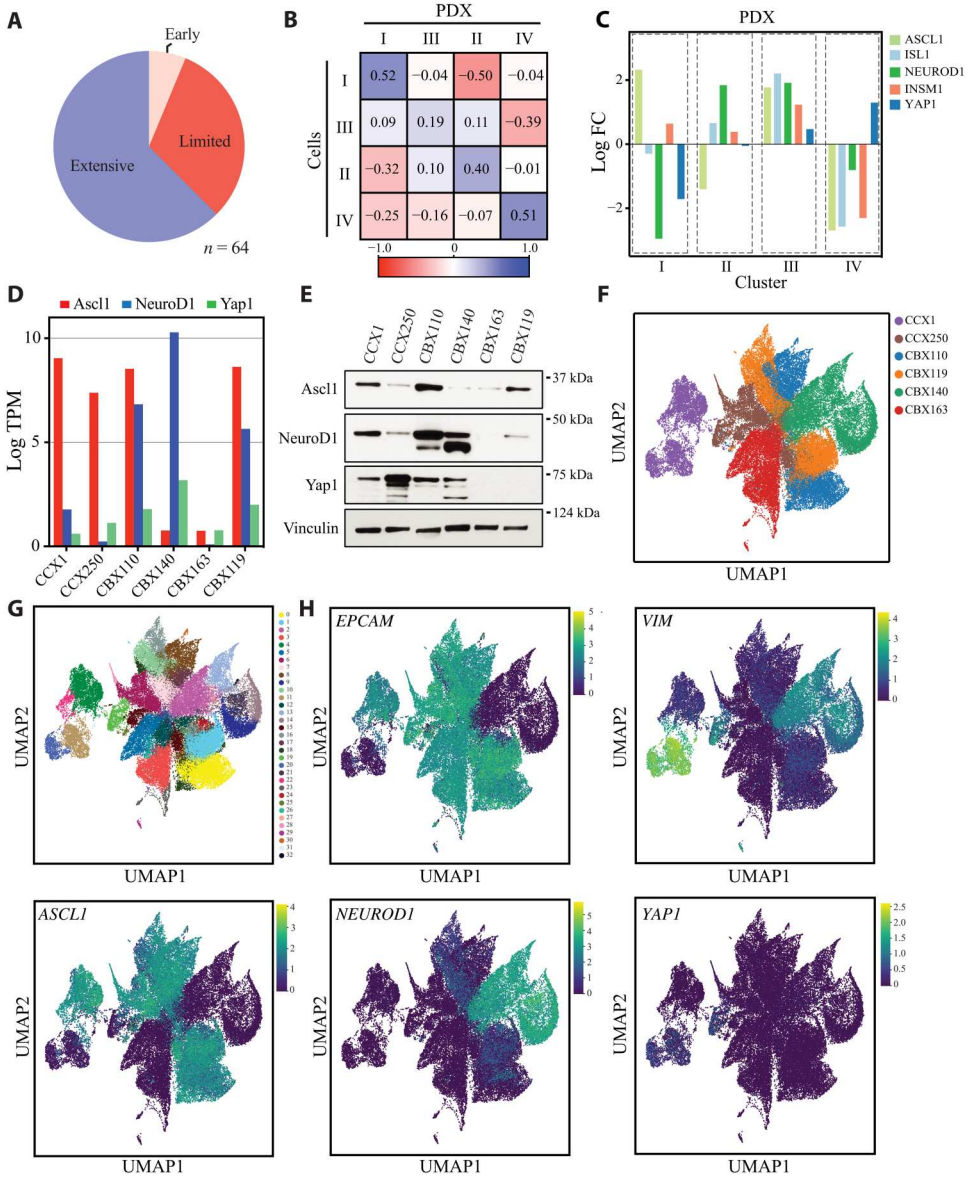

Fig. 2. The intratumoral heterogeneity of SCLC PDXs. (**A**) Clinical stage proportions of donor patients using a modified version of the Veterans Administration Lung Group criteria for SCLC. "Early" represents a subset of limited-stage disease without gross nodal involvement; these patients underwent surgery. (**B**) The association of the cluster-specific centroids of the shared genes between the cell line and PDX clusters was measured using the 1-Pearson. (**C**) The log fold change for fate-defining TFs in the indicated cluster versus the rest. (**D**) *ASCL1*, *NEUROD1*, and *YAP1* gene expression in the designated PDX was measured using RNA-seq. The corresponding PDX cluster for each sample is as follows: CCX1 (I), CCX250 (II), CBX140 (II), CBX119 (III), CBX110 (III), and CBX163 (IV). (**E**) Immunoblot analysis for relative expression of each TF in the designated PDX. (**F** to **H**) UMAP feature plots derived from scRNA-seq of the same six samples in (D) and (E) grouped by (F) sample ID, (G) Leiden clusters, and (H) the normalized expression of the designated genes.

retaining a median of 9672 and 3643, respectively, indicating the high-quality of our dataset. The population-level controls correlated with the averages of the single cells, Pearson r = 0.77 [95% confidence interval (CI), 0.75 to 0.77; P = <0.0001] (fig. S9).

Consistent with single-cell analyses in other tumor types, most individual cells varied more between than within individual tumors (*38*). Nevertheless, there were multiple examples of cells from individual tumors that occupied discrete regions of the Uniform Manifold Approximation and Projection (UMAP) coordinate map. Some tumors contained large groups of cells (e.g., CBX110, CBX119, and CCX250) that were more similar to other tumors than the within tumor population, consistent with the maintenance of intertumoral transcriptional programs. Feature plots of mesenchymal, epithelial, neural, and neuroendocrine markers confirmed that most SCLC cells comprised transcriptional programs represented by either epithelial or mesenchymal lineages (*EPCAM* or *VIM*, respectively) that further stratified into cells that express Ascl1, NeuroD1, or Yap1 (Fig. 2, F to H, and fig. S10). In contrast to previous single-cell RNA-seq (scRNA-seq) data (*39*), two profiled samples (CCX1 and CCX250) had a considerable number of

YAP1-expressing cells, and another (CBX140) had some cells with *YAP1* expression, although they were fewer and more dispersed across the UMAP space. Critically, although cells representing each TF were present in most tumors, the relative proportion of each marker within individual tumors was distinct across samples (see fig. S10).

SCLC tumors have discrete cell states regulated by the epigenome

To study *ASCL1*, *NEUROD1*, or *YAP1* expressing subpopulations in real time, we disaggregated PDX tumors and cultured derivative cells ex vivo in low-serum medium. Ex vivo cultures retained transcriptional fidelity with matched PDX across five tumors: CCX1, CCX280, CBX41, CBX163, and CBX140 (Pearson r = 0.88 to 0.96) (fig. S11). There was sufficient primary tumor sample to assess transcriptional fidelity of CCX1 primary tumor with matched PDX and ex vivo cells. CCX1 PDX and ex vivo samples were highly correlated with the transcriptome of the primary tumor (Fig. 3A). Relevant to the maintenance of subpopulation proportions ex vivo compared to in vivo, *ASCL1*, *NEUROD1*, *YAP1*, and associated gene expression were significantly correlated across five matched PDX and ex vivo cells (Pearson r = 0.74) (Fig. 3B). These results indicated that SCLC TF states were fundamentally preserved compared to in vivo tumors.

Bright-field microscopy of cells derived from CCX1 (Fig. 3C) and other ex vivo samples (fig. S12) demonstrated distinct cell types in strata. Live-cell imaging of the ex vivo culture indicated substantial interactions between the distinct compartments and putative cell type switches (movies S1 to S3). Strata of CCX1 were amenable to fractionation using physical and enzymatic means (see Materials and Methods). We compared protein expression of fate-determining TFs across the fractionated layers of CCX1 (Fig. 3D). Ascl1, NeuroD1, Yap1, and their associated genes were differentially expressed across each layer. The strata mirrored some of the molecular characteristics of established cell lines across distinct clusters (Fig. 1). The intratumoral subpopulations of CCX1 included (i) suspended aggregates (S^{++}) of small cells expressing Ascl1, (ii) semi-adherent groups of cells (S^{+}) expressing NeuroD1 that appeared to give rise to S^{++} aggregates, (iii) pleiomorphic adherent cells with neural-like projections (A^{+}), and (iv) tightly adherent mesenchymal-like cells growing as a monolayer (A^{++}) and expressing Yap1. Consistent with Western blot data, cell surface proteins CD44 and epithelial cell adhesion molecule (EpCAM) separated into adherent (A^{++}) and suspension compartments (S^{++}), respectively, as measured by flow cytometry (Fig. 3E). Together, these results indicated that individual SCLC tumors have the capacity to express three distinct TF-defined cell states concurrently and that these populations are in physical proximity ex vivo, suggesting an interactive intratumoral system. In support of this framework, Yap1-expressing cells, as measured by IHC in matched primary and PDX tissue, were at the interstices of Ascl1-expressing cellular sheets (fig. S13).

CCX1 comprised at least three cell states with distinct morphologies and significant cell-cell communication. We assessed the traits of the distinct compartments using physically separated strata or by flow cytometry ($CD44^{+}$ or $EpCAM^{+}$ cells) and examined cellular invasion, response to chemotherapy or radiation, and clonogenicity. Our results indicated that the A^{++}- or $CD44^{+}$-expressing cells, but not the other strata or $EpCAM^{+}$ cells, had the capacity to invade Matrigel (Fig. 3F). $CD44^{+}$ cells were also more resistant to chemotherapy and radiation (Fig. 3G). We noted that despite significant fluctuation from baseline in the proportion of $EpCAM^{+}$ and $CD44^{+}$ cells after therapeutic stress, cellular proportions as measured by each marker returned to pretherapy levels. These results indicated that cell state proportions were elastic but ultimately resilient to perturbation. As it related to clonogenicity, $EpCAM^{+}$ cells had a greater tumorigenic capacity than $CD44^{+}$ cells by both in vivo limiting dilution and in vitro colony formation assays (Fig. 3, H and I), in line with previous data (*40*). We demonstrate analogously distinct morphological and phenotypic characteristics in tumor subpopulations in another ex vivo sample, CBX140 (fig. S14).

To assess the extent that the epigenome regulates distinct subpopulations in CCX1, we conducted Assay for Transposase-Accessible Chromatin using sequencing (ATAC-seq) in each stratum (Fig. 3J). CCX1 strata had preferential accessibility at *ASCL1*, *NEUROD1*, and *YAP1* loci in a manner consistent with protein levels (see Fig. 3D), indicating that the expression of fate-determining TFs was regulated by the epigenome. To assess genetic diversity, we conducted whole exome sequencing of the bulk population and each stratum (fig. S15). The bulk population and each stratum had clonal *RB1* and *TP53* mutations/loss, indicating the human and malignant origin of each subpopulation. Moreover, the bulk population and the strata shared similar clonal architectures and genetic alterations [single-nucleotide variant and copy number alterations (93.8% similar)], indicating that successive waves of cellular expansion and selection did not result in diverse subclonal populations (*41*). Together, these results indicated that the distinct strata in CCX1 are regulated by nongenetic (epigenetic) processes.

Cell state dynamics indicate multivalent lineage plasticity

Our results indicated that most SCLC tumors contain two or more cell types and that intratumoral subtypes may cooperate to promote tumorigenicity and/or cellular diversity. Although bright-field live-cell imaging suggested cell type switches (movies S1 to S3) and RNA velocity estimates suggested some putative transitions between cell populations (fig. S16), we sought to measure SCLC TF subtype switching directly to quantify individual transition rates. We developed a fluorescent reporter platform that can measure TF states at the population and single-cell level. We generated reporter constructs containing the promoter sequence of *ASCL1*, *NEUROD1*, or *YAP1*. The inserts were placed upstream of reporter genes mCherry red fluorescent protein (mRFP), cyan fluorescent protein (CFP), or enhanced green fluorescent protein (eGFP) (Fig. 4A). Cells expressing each TF as measured by the corresponding fluorescence were morphologically distinct at the population and single-cell level and in their localization within strata (Fig. 4, B and C). *ASCL1* cells were round and mainly found in semi- or fully suspended cellular aggregates (S^{++}). *NEUROD1* cells represented the rarest subtype and comprised two main populations of very small round cells or more pleomorphic neural-like cells, and these cells were found mainly in emergent semisuspended aggregates (A^{+} and S^{+}). Last, *YAP1*-expressing cells were found mainly in the tightly adherent layer (A^{++}). Measurements of the aspect ratios (Fig. 4D) and cellular displacement (Fig. 4E) supported these characterizations insofar as *NEUROD1*- and *ASCL1*-expressing cells had greater sphericity and *YAP1*-expressing cells were irregularly shaped and had the greatest displacement.

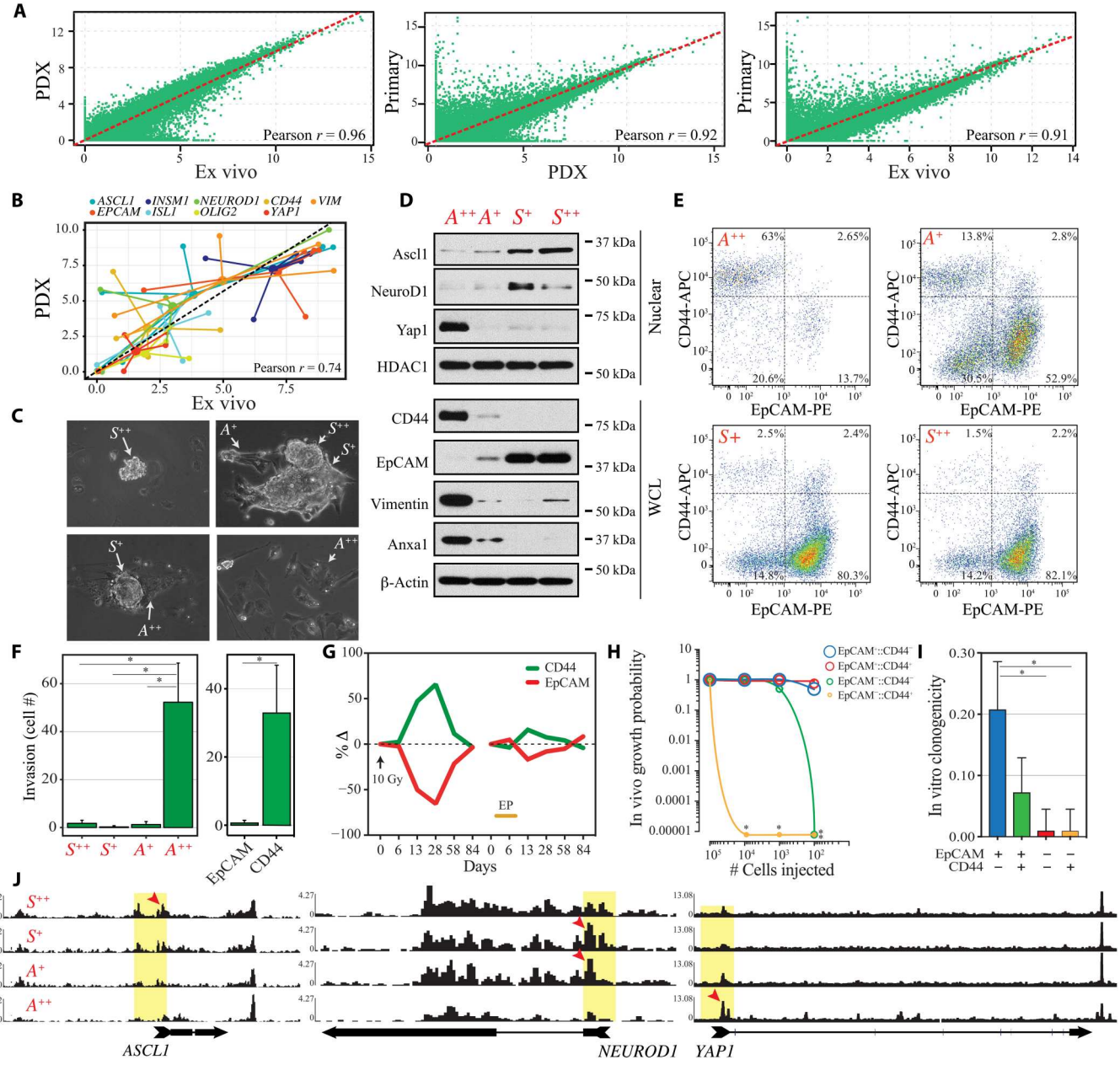

Fig. 3. SCLC ex vivo tumors have distinct phenotypic states regulated by the epigenome. (**A**) Whole transcriptome associations in matched CCX1 primary tumor, PDX, and ex vivo cells. (**B**) Scatter star plot of gene expression [transcript per million (TPM)] for program defining genes in five matched PDX and ex vivo cells: CCX1, CCX280, CBX41, CBX163, and CBX140. Hubs = means; spokes = individual sample values. (**C**) Phase contrast images (×20) of CCX1 ex vivo cells. Arrows mark representative populations of cells in each stratum. (**D**) Strata profiled by immunoblot. (**E**) Flow cytometry data show CD44- and EpCAM-expressing cells in each stratum. APC, allophycocyanin; PE, phycoerythrin. (**F**) Invasion assay of strata or cells sorted via fluorescence-activated cell sorting (FACS) for CD44 or EpCAM. Values are an average of the number of stained cells from four high-power fields. Error bars represent SEM of at least three different experiments. The student *t* test with Welch's correction was used for statistical analysis. **P* < 0.05. (**G**) CCX1 ex vivo cells (5×10^6) were treated with chemotherapy (EP; etoposide (1.5 μg/ml) and cisplatin (0.5 μg/ml)] for 5 days, followed by drug washout or irradiated to a total dose of 10 Gy (2 Gy per fraction daily). CD44- and EpCAM-expressing cells were quantified by flow cytometry at the indicated times, and the change in the percentage of CD44 and EpCAM (%Δ) calculated relative to *t* = 0. (**H** and **I**) Cells with differential expression of EpCAM and CD44 expression were FACS-sorted and tested for clonogenicity in vitro or in vivo (limiting dilution assay). Tumor growth was followed for ~8 weeks in NOD.Cg-*Prkdc*^{scid} *Il2rg*^{tm1Wjl}/SzJ (NSG) mice. *Nonoverlapping CIs of the proportions as calculated by the Clopper and Pearson exact test. (**J**) Track plots of ATAC-seq signals at the *ASCL1*, *NEUROD1*, and *YAP1* loci in each stratum of CCX1. Red arrowheads and yellow shading mark accessibility and the designated promoters, respectively.

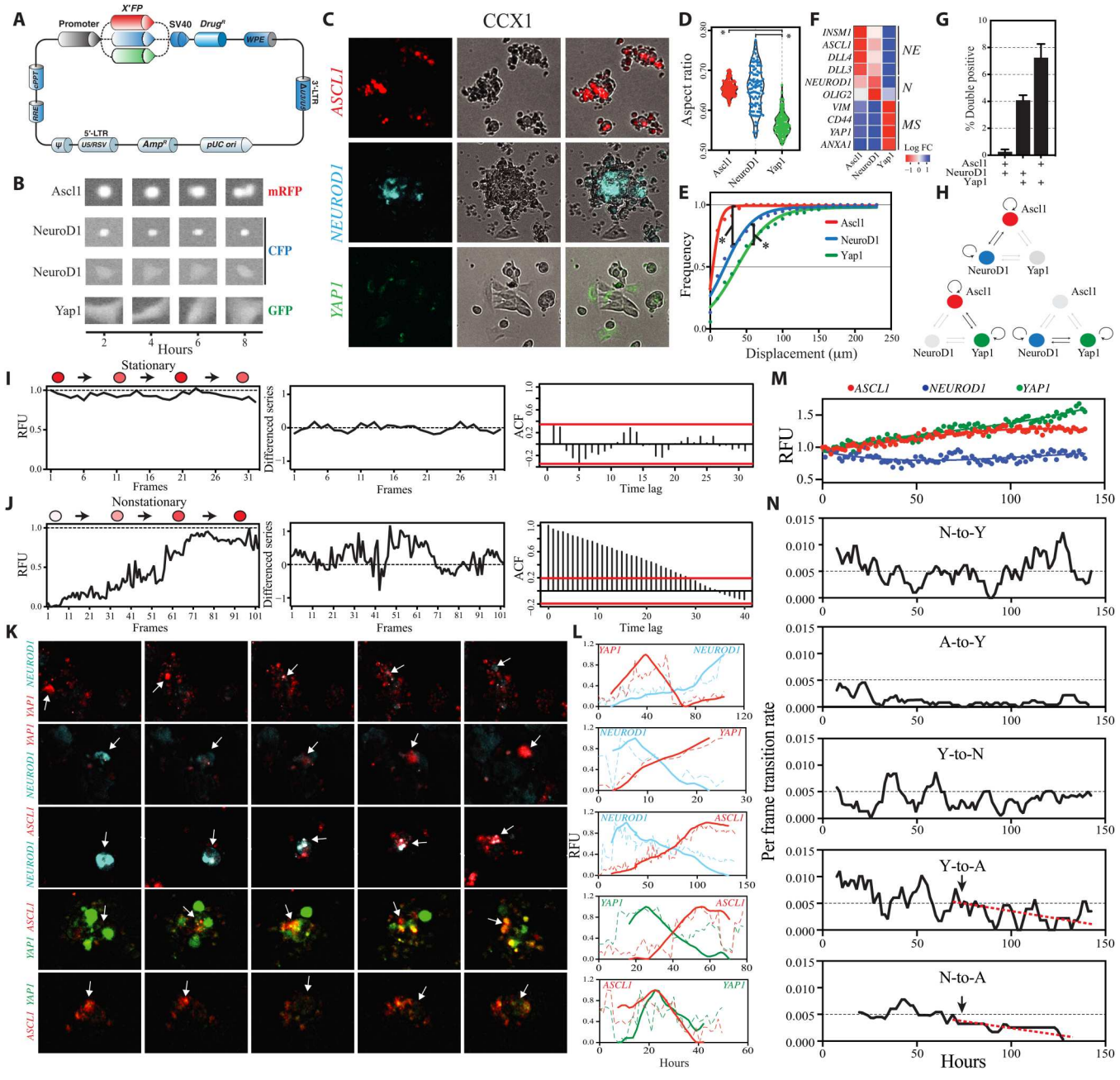

Fig. 4. Quantifying cell state transitions by single-cell fluorescence tracking. (**A**) Schematic of a TF reporter vector. Sequences flanking the promoter of each gene were placed upstream of the ORFs of the FPs (*X′FP*). WPE, Woodchuck Hepatitis Virus Posttranscriptional Element; RRE, Rev responsive element; cPPT, central polypurine tract; 5′LTR, 5′ long terminal repeat; U5/RSV, inverted repeat within the U5 region of the Rous sarcoma virus; AmpR, ampicillin resistance gene; pUC ori, the pUC plasmid's origin of replication. (**B**) Representative tracks of cells expressing the indicated reporters. (**C**) Representative fluorescent, bright-field, and merged images of cells expressing the indicated reporters. (**D**) Aspect ratios of fluorescent cells are shown by violin plots. *$P < 0.05$, Mann-Whitney test. (**E**) Cumulative distribution function of displacement of fluorescent cells. *$P < 0.05$, Mann-Whitney test. (**F**) Log fold change of flow cytometry separated fluorescent versus nonfluorescent cells from single reporter transfected populations for neuroendocrine (NE), neural (N), and mesenchymal (MS) genes. (**G**) Cells expressing two reporters (i.e., double positive) were detected using flow cytometry. (**H**) Schematic depicting all possible transitions using bivalent reporter integration. Serial fluorescent measurements of a representative stationary (**I**) and nonstationary (**J**) cells. Differenced series represent the computed differences between two consecutive measurements. Autocorrelation (ACF) was measured by calculating the correlation of the time series with itself at variable time lags. Red bars indicate 95% CI. (**K**) Representative dual fluorescent images of cell state transitions observed in CCX1 ex vivo cultures. Arrows mark the transitioning cells. (**L**) Serial fluorescent measurements of corresponding transitions in (K). RFU per frame and moving averages (every 10 frames) are shown as dashed and solid lines, respectively. (**M**) Total fluorescence for each TF reporter, over time. (**N**) The instantaneous transition rates for the state transitions in CCX1 were measured from at least 150 hours of live-cell imaging. Lines represent the moving average of every five frames. Arrows corresponding to the plateau phase of *ASCL1*-expressing cells in (M) are shown in the Y-to-A and N-to-A panels. Linear regression of the transition rates are shown with red dashed lines.

To determine whether reporter positive cells expressed the corresponding TF states, we separated fluorescent and nonfluorescent cells from single reporter transfected populations using flow cytometry and measured the relative enrichment for each TF and coregulated genes by bulk RNA-seq. We observed enrichment of TF and associated gene transcripts for each reporter (Fig. 4F), suggesting that each TF reporter marks the corresponding lineage with high fidelity.

To quantify transitions between TF states, we generated cells expressing dual reporters by tandem transfections. We observed populations of cells expressing one or the other reporter with minimal coexpression in individual cells (Fig. 4G). These results, which are consistent with the minimal overlap of TF gene expression seen in individual cells in scRNA-seq UMAP plots (Fig. 2H), suggest that cell states are largely mutually exclusive. These results are also consistent with recently published SCLC scRNA-seq data (*39*). Tandem, tripartite transfections were either lethal or resulted in prohibitively slower growth, precluding trivalent measurements. Nonetheless, we used a permuted bivalent approach to measuring all possible state transitions (Fig. 4H). The percentage of mRFP, eGFP, and CFP in either monovalent or bivalent reporter transfections was similar: 77 ± 5% *ASCL1*, 12 ± 3% *YAP1*, and 5 ± 1% *NEUROD1* (means ± SD) and approximated the scRNA-seq TF expression in CCX1 (Fig. 2H). These results indicated that our bivalent TF reporter systems accurately mark distinct subpopulations.

We used automated single-fluorescent reporter tracking to follow individual cells transfected with bivalent reporters via time-lapse imaging. We generated single-cell tracks from up to 250 hours of live-cell images for our ex vivo samples and measured relative fluorescence unit (RFU) intensity per cell per frame. We identified two distinct signal processes. Cells either emitted signals characterized by variable fluctuations but with a mean, variance, and covariance that did not change with time (i.e., stationary; Fig. 4I), or they were nonstationary (Fig. 4J). The latter had a discernible trend in fluorescence intensity (increase or decreasing) and a statistically significant time lag autocorrelation (Fig. 4, I and J). To mitigate against the risk of capturing spurious transitions, we adopted a stringent signal processing heuristic. This consisted of statistically significant autocorrelation signals of concomitantly vanishing and emerging cell states for each tracked particle. Bivalent transitions were quantified using dual reporter time series analysis (Fig. 4K and movies S4 to S8). Representative state transitions from cropped frames in time series are shown in Fig. 4L. We applied these criteria to CCX1 cells cultured from 10^5 cells to ~80% confluency and assessed state transitions as a function of density (Fig. 4M). We calculated a per frame state transition rate, defined as the number of state transitions between two sequential frames, captured 1.5 hours apart, divided by the total number of cells in the secondary frame (Fig. 4N). Our results indicated variable moving average frequencies across the six possible state transitions. Notably, direct Ascl1 to NeuroD1 state transitions either did not occur or were lower than the limit of detection in this tumor (although this transition was observed in other samples; see Fig. 5). Moreover, as the population approached near confluency, there were notable changes in some transition rates. Namely, there was a decrease in the transitions into Ascl1 (arrows in Fig. 4N), which corresponded to the plateau phase of growth of the Ascl1 population. These results suggested that transition rates can potentially be modulated to configure tumor composition in a manner responsive to environmental stressors (e.g., higher cellular density, lower pH, or lower nutrient state). Together, SCLC tumors can interconvert between different TF states, and some transition rates are altered in response to environmental cues.

Individual CCX1 cellular interconversions appeared to occur randomly (Fig. 4N), and the tumor population was resilient to change after therapeutic stress (Fig. 3G). These features suggested that state dynamics in this tumor were governed by a stochastic process. Markov chains have been used to model pseudo-randomly changing systems and infer transition probabilities between phenotypic states within cancer cell populations (*4*). A prediction of Markov state dynamics is that any state will return to a fixed equilibrium of cell state proportion over time if transitions are multivalent (i.e., transitions can occur between any two states). To assess these properties in CCX1, cells with integrated bivalent reporters were purified (via flow cytometry) into homogeneous states and followed by serial fluorescence measurements (fig. S17 and Supplementary Materials and Methods). *ASCL1*, *NEUROD1*, or *YAP1* purified states evolved over time to invariably express the other reporter. Using serial matrix proportion measurements, we estimated the transition probability (P) for each of the nine possible transitions and estimated the equilibrium cell state composition using $I^{(eq)}$. We then measured the proportions of each reporter in experimentally unperturbed (unsorted) populations over 7 days. The experimentally measured proportions were highly correlated to the estimated equilibrium state composition (fig. S17D), indicating that state dynamics can be accurately predicted by a Markov chain (*42*).

To determine the associations between state transitions and the intratumoral composition of SCLC tumors, we generated TF reporter–expressing cells in three additional SCLC tumors and one NSCLC tumor, CCX29 (Fig. 5A). Expectedly, CCX29 expressed *YAP1* but not *ASCL1* or *NEUROD1*. We observed distinct intratumoral compositions (Fig. 5B), and state transition rates varied across the four tumors (Fig. 5C). We measured the transition probabilities using single-cell tracking for each sample and predicted the equilibrium state proportions using Markovian chain processes (see Supplementary Materials and Methods). The predicted and measured state proportions were highly correlated (Pearson $r = 0.82$) (Fig. 5D). To assess the magnitude of the dependence of intratumoral proportions on state transitions, we simulated changes in individual transition rates and assessed the impact on each TF state (Fig. 5, E and F). These results indicated that cell state transitions are critical for regulating SCLC intratumoral compositions. Moreover, simulated changes in specific transitions (e.g., between Yap1 and NeuroD1 in CCX280; Fig. 5F) had more impact on tumor compositions than other transitions, and these dependencies varied in a tumor-specific manner (fig. S18).

Our data on SCLC state dynamics indicated that transitions regulate intratumoral composition. Since each state had distinct functional attributes, we reasoned that the prevalence of each state in individual tumors may influence clinical outcomes. We annotated clinical outcomes from the 64 donor patients (table S1 and data S3). First, we examined known variables of SCLC outcomes. For example, both cancer stage (limited versus extensive) and the use of chemotherapy were significantly associated with overall survival, and the use of chemotherapy was significantly associated with progression-free survival (fig. S19). These associations suggested that salient variates that influence outcomes could be identified using

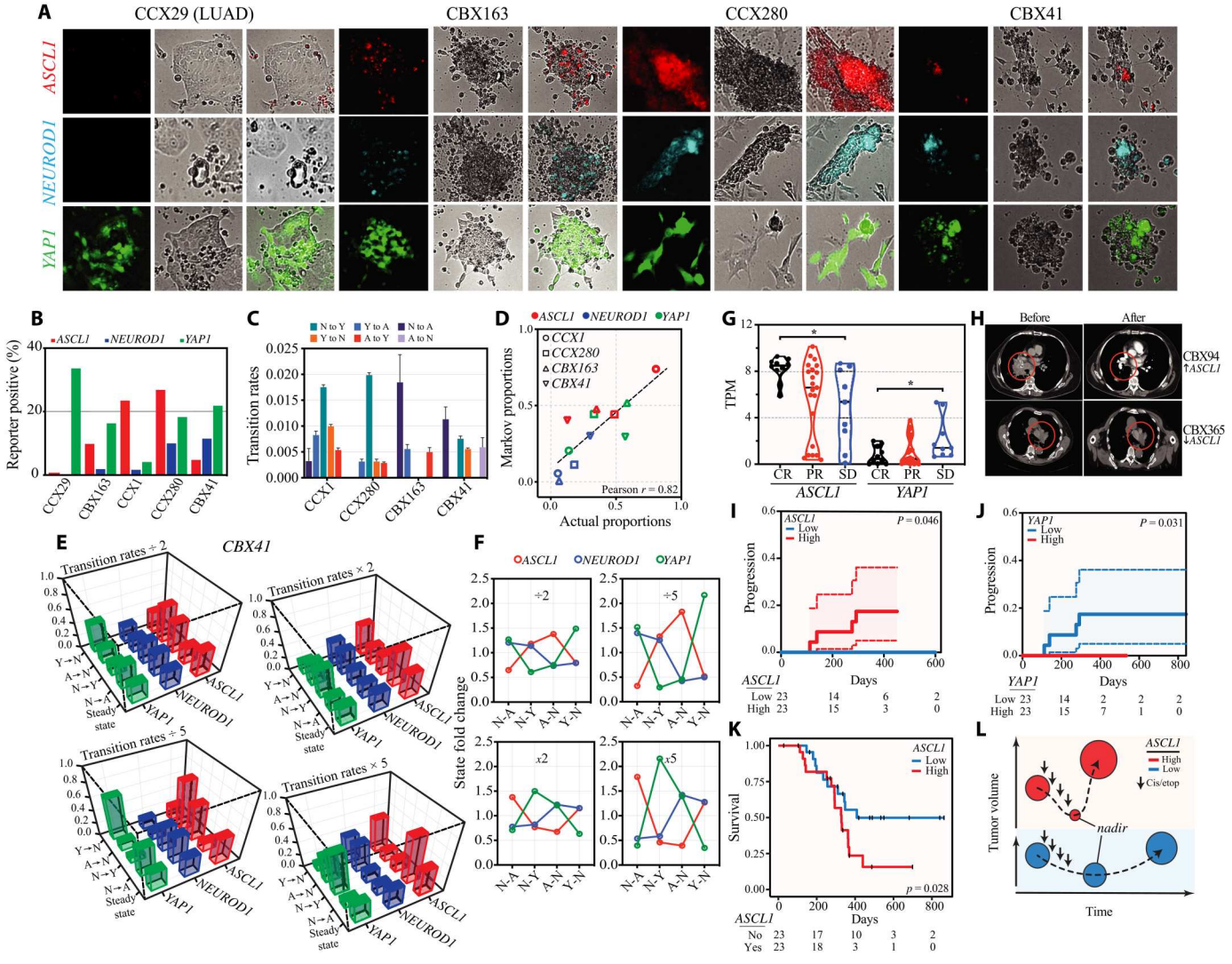

Fig. 5. SCLC composition is regulated by stochastic cell state transitions and is associated with distinct clinical response trajectories. (**A**) Representative fluorescent, bright-field, and merged images from cells with *ASCL1*, *NEUROD1*, or *YAP1* reporters across four ex vivo tumors. CCX29 was derived from a lung adenocarcinoma (LUAD). (**B**) Proportion of reporter expression (% reporter positive). Data are representative of three additional images for each ex vivo tumor. (**C**) The transition rates for all possible transitions were calculated by averaging instantaneous transition rate measures from at least 150 hours of live-cell imaging. Error bars represent SEM of transition rates from four high-power fields in at least two wells. (**D**) Scatterplot of state proportions measured experimentally (*x* axis) or at equilibrium using the Markov chain (*y* axis). Estimates of CBX41 ex vivo tumors state (**E**) proportions and (**F**) fold change upon variance of transition rates by the indicated values. (**G**) PDX-sourced *ASCL1* and *YAP1* gene expression levels stratified by treatment response after first-line chemotherapy ± radiation. CR, complete response; PR, partial response; SD, stable disease. Bars represent the median, and the Mann-Whitney test was used for statistical analysis. *$P < 0.05$. (**H**) Representative patient computed tomography images before and after induction chemotherapy comprising 4 cycles of etoposide and carboplatin. High and low *ASCL1* expressions were median stratified using TPM. Red circles delineate the gross tumor volume. Estimated cumulative incidence curves of tumor progression stratified by (**I**) *ASCL1* or (**J**) *YAP1* gene expression. Shaded area represents 95% CI. (**K**) Kaplan-Meier estimates of overall survival of patients stratified by median *ASCL1* gene expression. (**L**) Schematic illustrating distinct chemotherapy (cis/etop) response trajectories for *ASCL1* high or low tumors.

this dataset. We then combined TF expression as measured by bulk RNA-seq with clinical outcomes. Tumors with high *ASCL1* or *YAP1* expression were more and less likely to respond to first-line chemotherapy ± radiation, respectively (Fig. 5, G and H). Moreover, tumors with relatively higher *ASCL1* expression, despite having higher response rates after first-line therapy, were significantly more likely to ultimately progress ($P = 0.046$; Gray's test for equality based on competing risk of death) and concomitantly had a worse overall survival ($P = 0.028$; log-rank test) (Fig. 5, I and K). Conversely, tumors with relatively higher *YAP1* expression were less likely to progress after chemotherapy ($P = 0.021$; Gray's test for equality based on competing risk of death) (Fig. 5J). Therefore, state composition had a significant impact on chemotherapy response. A schematic describing tumor response trajectories after chemotherapy stratified on the basis of *ASCL1* expression is shown in Fig. 5L.

Epigenetic modifiers reconfigure SCLC intratumoral states

SCLC TF state transitions were stochastic, modulated by the environment (i.e., cellular density), and appeared regulated by epigenetic processes (Fig. 3J). Accordingly, we reasoned that intratumoral state proportions can be altered using drugs that target the epigenome. We assessed the impact of distinct classes of epigenetic drugs on CCX1 morphology using longitudinal treatments at sublethal doses (fig. S20). We tested drugs that were U.S. Food and Drug Administration–approved, currently in clinical trials, or pending examination in trials: MS-275, GSK2879552, SAHA, iBET-726, JIB-04, and EPZ6438. Most drugs appeared to differentially impact subpopulation growth. In particular, JIB-04, which inhibits the Jumonji family of histone demethylases, diminished the growth of suspended cell aggregates (i.e., S^{++} or neuroendocrine cells) (Fig. 6A). Conversely, iBET-762, a small-molecule inhibitor that targets bromodomain and extra terminal (BET) proteins, promoted suspended cell aggregate growth while decreasing adherent cell growth (i.e., A^{++} or mesenchymal cells). We used TF reporter–expressing cells to assess the impact of JIB-04 and iBET-762 on TF expression. Consistent with the bright-field microscopy findings, JIB-04 decreased *ASCL1*-expressing cells and had moderate to minimal effects on *YAP1* and *NEUROD1* expression (Fig. 6B). Conversely, iBET-762 increased *ASCL1*, reduced *YAP1*, and did not significantly alter *NEUROD1* expression. Morphometric analyses of TF-expressing drug-treated cells demonstrated distinct morphological states. iBET-762 and JIB-04 increased the number of equiaxed (spherical) and elongated (asymmetric) cells, respectively (Fig. 6C). To assess the impact of each drug on the transcriptome, we performed scRNA-seq and showed that drug treatments lead to divergent cell types (Fig. 6D). Namely, iBET-762 increased the number of *EPCAM*- and *ASCL1*-expressing cells and significantly decreased the number of *VIM*-, *CD44*-, and *YAP1*-expressing cells. JIB-04 had diametrically opposed effects in CCX1. To quantify these effects, we visualized *ASCL1*, *NEUROD1*, and *YAP1* transcript levels per cell by density distribution plots (Fig. 6E). Therefore, JIB-04 and iBET-762 significantly altered the prevalence of each TF state.

To determine whether the changes in CCX1 composition by JIB-04 and iBET-762 were attributed to modulations in cell state transition rates, we quantified single-cell transitions using dual reporter time series analyses of CCX1 cells treated with sublethal doses of drug (Fig. 6F). Specifically, we used concentrations that had a maximal growth inhibition of ~10% for any state in an individual tumor at day 10. We calculated the average transition rate using generated single-cell tracks from up to 250 hours of live-cell images. Our results indicated an increase in *NEUROD1* to *ASCL1* transitions after iBET-762 treatment and a decrease in bilateral *NEUROD1* to *YAP1* transitions. These changes in state transitions are consistent with the reconfiguration of this tumor toward a more neuroendocrine ($Ascl1^{+}$) composition. Despite a retention of some Yap1-expressing cells in JIB-04–treated cells (see Fig. 6B), there were no significant transitions observed under these conditions.

To assess the extent that the observed reconfiguration of tumor proportions was attributed to differential cell death, we measured the absolute number of dead cells using 4′,6-diamidino-2-phenylindole (DAPI) staining in longitudinally treated cultures treated with vehicle or drugs (iBET-762 and JIB-04). *ASCL1*-expressing cells had a higher basal rate of death than *YAP1*-expressing cells, followed by *NEUROD1*-expressing cells (fig. S21). However, in the setting of the use of sublethal concentrations of the indicated drug, the number of dead cells was not significantly higher across the three states. These results indicated that tumor composition reconfiguration under these conditions is not attributed to differential drug-induced death.

We also measured the change in CCX1 composition by JIB-04 and iBET-762 in other tumors. We measured a surrogate marker of the neuroendocrine state, suspended cell aggregates (or S^{++}) in five additional ex vivo samples (Fig. 6F). Although the magnitude of changes varied across samples, iBET-762 and JIB-04 appeared to increase and decrease cluster size, respectively. These results suggested that although each tumor has preferred state proportions at equilibrium, intratumoral composition can be modulated using drugs that target the epigenome.

CBX41, in particular, had a significant increase in suspended cell aggregates in the presence of iBET-762 (Fig. 6F). To determine the basis of this change in phenotype, we examined TF state composition in this sample. In contrast to CCX1, CBX41 had a lower number of *ASCL1*-expressing cells, with moderate-to-high *NEUROD1* and *YAP1* expression at baseline (Fig. 5B). We used the TF reporters to assess the impact of iBET-762 on TF expression in CBX41 (Fig. 7A). iBET-762 increased *ASCL1* and decreased *NEUROD1* and *YAP1*, compared to vehicle-treated cells. *ASCL1* reporter fluorescence images in conjunction with bright-field images demonstrated a significant increase in *ASCL1* expression after iBET-762 (Fig. 7B). As shown in Fig. 6F, iBET-762 increased the growth of suspended cell aggregates (i.e., S^{++} or neuroendocrine cells). These results suggested that the increased growth rate in CBX41 after iBET-762 treatment is due to a change from a *NEUROD1* to an *ASCL1* tumor composition. To examine this treatment effect on the protein level, CBX41 ex vivo cells were treated with iBET-762 for 3 or 5 days. Western blot analyses showed an increase in Ascl1 and a decrease in NeuroD1 levels at 3 and 5 days after treatment (Fig. 7C). Quantification of band intensity demonstrated a significant increase in the Ascl1:NeuroD1 protein ratio after iBET-762 treatment (Fig. 7D). CBX41 xenografts were then injected into mice and treated with iBET-762. iBET-762 accelerated tumor growth compared to mock-treated controls (Fig. 7E). These results indicated that iBET-762 enhances the growth of CBX41 by reconfiguring tumor composition toward a more proliferative neuroendocrine state.

Epigenetic modifiers alter SCLC chemotherapy response trajectories

Since state composition had a significant impact on clinical responses to chemotherapy (see Fig. 5, G to L), we predicted that altering state proportions using JIB-04 or iBET-762 would also alter treatment responses in derivative PDXs. CCX1 and CBX41 were injected into mice and treated adjuvantly (Fig. 8A) or neoadjuvantly (Fig. 8B) with JIB-04 or iBET-762 and 3 cycles of cisplatin and etoposide. Adjuvant iBET-762 and JIB-04 significantly accelerated and decelerated tumor regrowth compared to chemotherapy alone in CCX1 (Fig. 8C). In CBX41, adjuvant iBET-762 had an accelerated recovery compared to adjuvant JIB-04 but not to chemotherapy. Neoadjuvant JIB-04 accelerated tumor regrowth compared to chemotherapy alone in both CCX1 and CBX41 (Fig. 8D). Neoadjuvant iBET-762 had subtle effects on treatment response trajectories in the two xenografts. In CCX1, which had a high proportion of Ascl1 at baseline (84% of all fluorescent cells; Fig. 5B), neoadjuvant

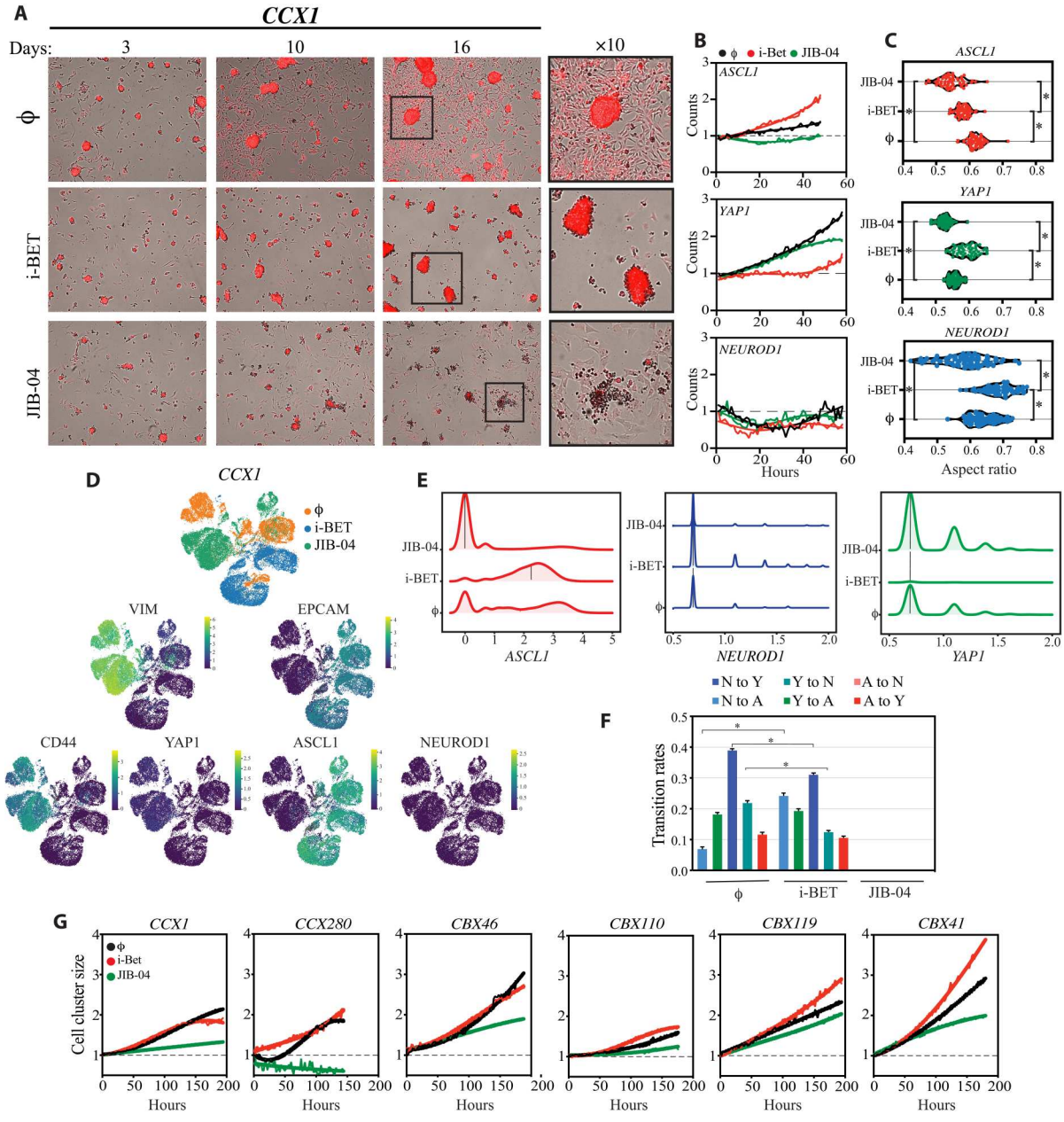

Fig. 6. Reconfiguring SCLC tumor composition by epigenetic reprogramming. A series of ex vivo tumor experiments (A to F) were performed involving treatment with iBET-726 (30 nM), JIB-04 (50 nM), or vehicle (ϕ). (**A**) Treated CCX1 ex vivo cells expressing RFP (for enhanced visualization of the adherent layer) were monitored for morphological changes for up to 16 days by bright-field and fluorescent images. Black boxes in the image at 16 days were magnified to ×10 (last column). (**B**) Fluorescent cells with integration of the designated reporter construct were counted longitudinally after treatment. The relative counts, normalized to the value at $t = 0$ hours, are shown. (**C**) The aspect ratios of these fluorescent positive cells are shown by violin plots, following treatment. The Mann-Whitney test was used for statistical analysis. *$P < 0.05$. (**D**) UMAP feature plots derived from scRNA-seq of treated CCX1 ex vivo tumors were grouped by (top) drug ID or (bottom) the normalized expression of the designated genes. (**E**) Density distributions comprising the normalized scRNA-seq gene expression values for treated CCX1 ex vivo cells. Black bars represent the medians. (**F**) The average transition rates for CCX1 ex vivo cells treated with iBET-762 (10 nM) or JIB-04 (10 nM). The Student t test with Welch's correction was used for statistical analysis. *$P < 0.05$. (**G**) Cell cluster size, as measured by the average size of suspended cellular aggregates per image (a surrogate of neuroendocrine subpopulations), was measured for six distinct ex vivo tumors following treatment.

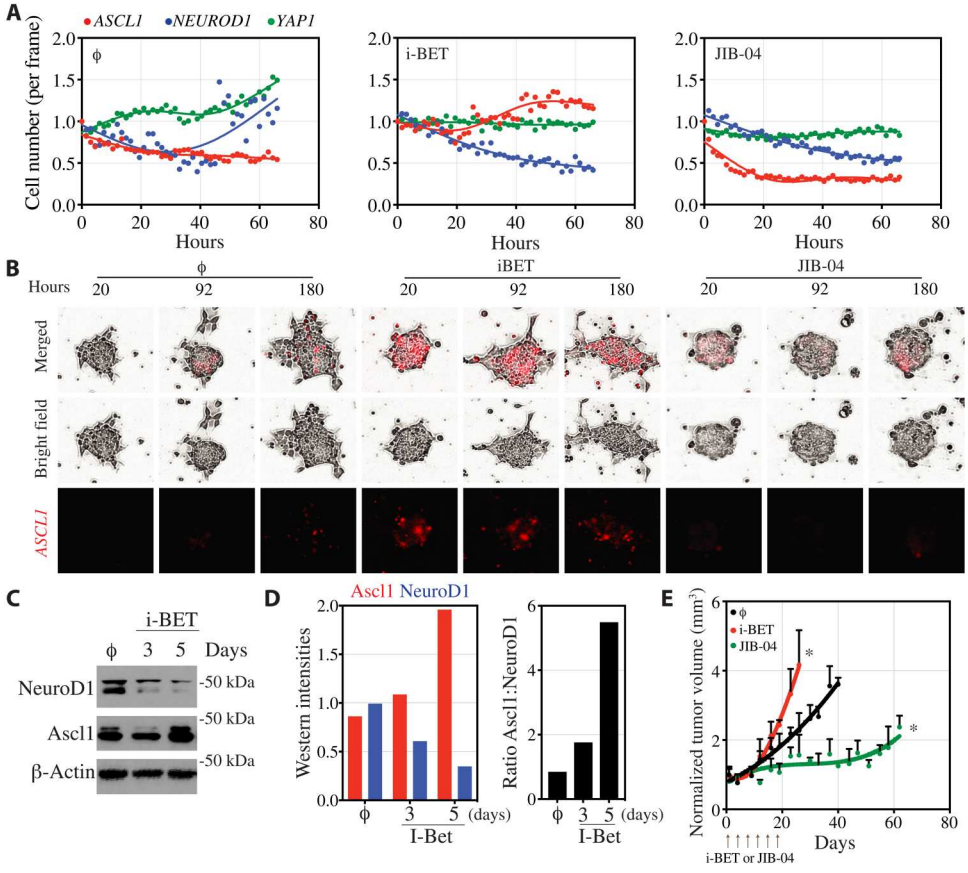

Fig. 7. Epigenetic reprogramming alters tumor phenotype. (**A**) Fluorescent CBX41 cells with integration of the designated reporter construct were counted longitudinally after treatment. (**B**) Representative fluorescent, bright-field, and merged images from cells with stable integration of the *ASCL1* reporter construct. (**C**) Immunoblot analysis for relative expression of NeuroD1 and Ascl1 after treatment. (**D**) Quantification of immunoblots in (C). (**E**) NSG mice bearing CBX41 in the flank were block randomized into one of three treatment arms as shown. Data are expressed as means ± SEM; $n = 4$ independent animals for each arm. The χ^2 test was used for statistical analysis. *$P < 0.05$. Arrows represent every other day dosing with iBET-762 or JIB-04 treatments.

iBET-762 did not significantly change tumor sensitivity to chemotherapy. In CBX41, which had low proportion of Ascl1 at baseline (13% of all fluorescent cells; Fig. 5B), neoadjuvant iBET-762 had a biphasic response trajectory with more rapid growth initially, followed by a lag in tumor regrowth compared to chemotherapy alone. Together, these results indicated that epigenetic drugs altered tumor chemotherapy response trajectories in a treatment sequence–dependent manner.

DISCUSSION

Despite some indications that individual SCLCs may comprise distinct cell types, the extent of human SCLC intratumoral heterogeneity and the direct observation of subtype switching has been elusive (*15*, *16*, *19*, *22*, *25*–*28*, *31*, *32*, *35*, *39*, *43*). In this study, we showed that treatment naïve SCLCs are substantially more heterogeneous than previously appreciated, with most samples retaining two or more cell types that can access transcriptional states marked by *ASCL1*, *NEUROD1*, or *YAP1*. We showed that the relative frequency of each state varied across tumors and that most SCLCs are governed by reversible bidirectional cell state transitions rather than unidirectional differentiation hierarchies. We conclude that there are stable attractors, or preferred states, in the gene expression network topology of most SCLC characterized by the expression of two or more state-defining TF genes.

We measured the kinetics of state transitions and associated single-cell dynamics with overall population trends using stochastic transition theory (i.e., Markov chains). Our results suggest that the transition rates in individual tumors have autonomous circuits that are critical for configuring intratumoral proportions. Despite a propensity toward an equilibrium in individual tumors, transition probabilities were affected by environmental signals including population density and drug treatments. These results advance a model whereby SCLCs represent multistate dynamical systems that are responsive to their environment.

Our findings introduce new questions about the regulation of state dynamics and tumor proportions. First, the per frame transition rates are on the order of 0.0 to 0.02 transitions per frame or 0 to ~1/50 cells every 1.5 hours. This represents a small fraction of each subpopulation. It is unclear whether the transitioning fraction is fixed or transitory and the extent that some cells undergo terminal differentiation (i.e., no longer retain the capacity to transition into other states) within each state is not currently known. Second, our findings suggest that SCLCs appear to contain intrinsic clocks that regulate cell state transitions. The source of this synchrony and its stochastic tendencies are not known. In bacteria, noise in

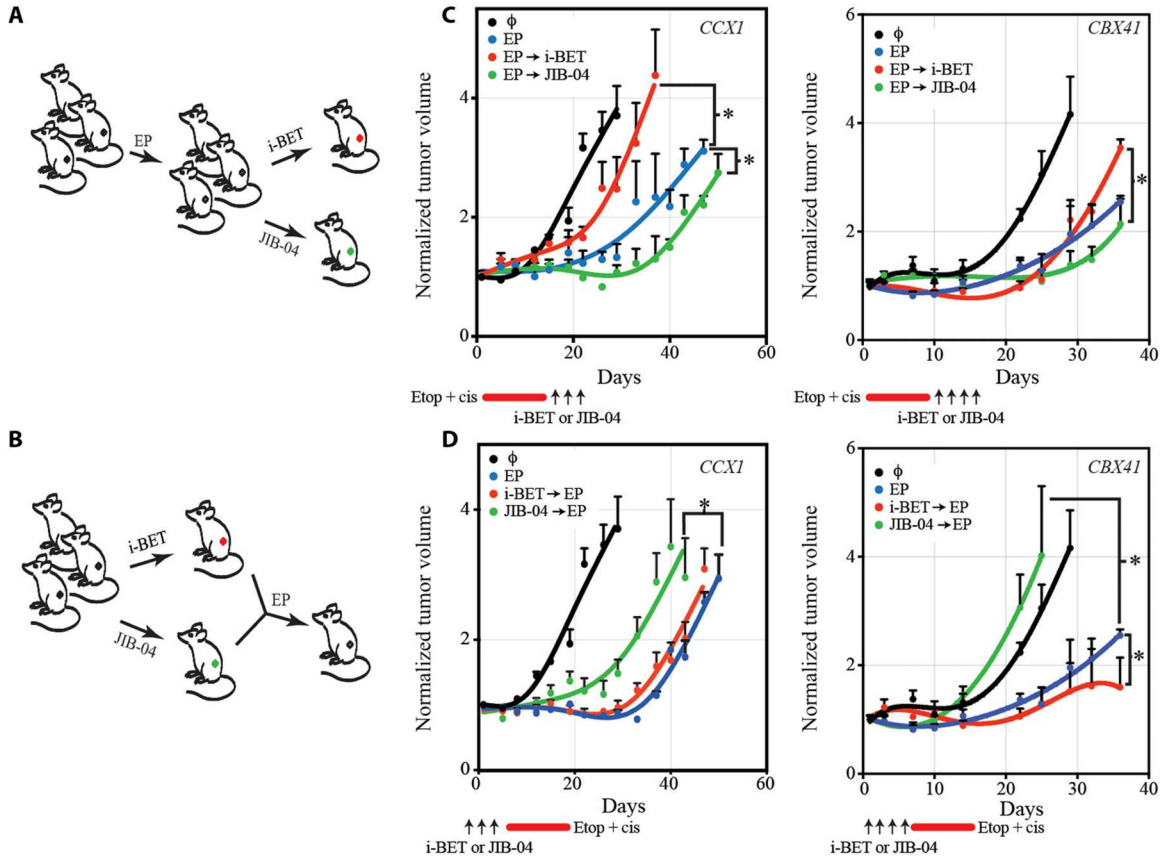

Fig. 8. Epigenetic reprogramming alters chemotherapeutic response trajectories. Schematics depicting (**A**) adjuvant and (**B**) neoadjuvant treatment strategies with iBET-726 or JIB-04. (**C** and **D**) NSG mice bearing CCX1 or CBX41 in the flank were block randomized into one of three treatment arms as shown. Sequential treatments were given at least 24 hours after the completion of the first therapy. Data are expressed as means ± SEM; $n = 4$ independent animals for each arm. The χ^2 test was used for statistical analysis. *$P < 0.05$. Arrows represent every other day dosing with iBET-762 or JIB-04 treatments. The red bar represents the duration of chemotherapy treatments.

underlying genetic circuits permits access to different dynamic regimes, including gene program oscillations that result in cellular differentiation (*44*). It is possible that tumor state transitions similarly depend on noise in the underlying gene regulatory networks. Third, in addition to the putative autonomous circuitry, certain environmental cues appear to influence the timing of these transitions. For example, the attenuation of conversion into the *ASCL1* state upon increased population density suggested that cell-cell or paracrine signals could influence transition probabilities, although the precise nature of these interactions remains unknown.

SCLC's state diversity is likely a major feature of its clinical versatility and lethality. Cell type diversity can confer several advantages in tumors including allowing subpopulations to foster the growth of another group. The cell-cell interactions observed between SCLC cell types suggest that these fostering exchanges are possible. Specifically, the extensive contacts observed between Yap1- and NeuroD1- or Ascl1-expressing cells suggest commensal niche-like interactions (see delimited areas in movies S1 to S3). In addition, phenotypic switching between therapy sensitive (neuroendocrine) and therapy-resistant states (mesenchyme or neural) is predicted to underlie SCLC's persistence despite significant initial responses to chemotherapy. Consistent with this observation, we showed that SCLCs had varied clinical and PDX chemotherapy treatment response trajectories in a manner dependent on the expression level of the *ASCL1* and *YAP1* states. We conclude that the nongenetic means to undergo transitions provides the capability for some tumors to swiftly reemerge once the therapy is withdrawn, a hallmark of SCLC clinical response trajectories.

There is evidence to support a role for the epigenome in the state diversity of SCLC. Namely, there was preferential promoter accessibility to *ASCL1*, *NEUROD1*, and *YAP1* in a manner similar to protein and phenotypic expressions in ex vivo strata. Despite the potential for gene promoter accessibility for each state, it is evident that there are differential epigenetic constraints in individual tumors since state proportions varied significantly in the cohort. Plastic epigenetic topologies may result from relaxation or restriction of epigenetic landscapes (*45*), which may enhance the evolutionary fitness of some SCLCs. It is also plausible that certain genetic alterations regulate epigenetic barriers and, accordingly, TF state proportions in tumors. For example, MYC activation has been shown to facilitate transitions from *ASCL1* toward *NEUROD1* or *YAP1* expression (*32*). Other putative variables for the regulation of the epigenome include genomic alterations in genes that regulate histones (e.g., *CREBBP*, *EP300*, and *MLL*), differential DNA methylation patterns, and distinct cells of origins (*14*, *20*, *46*).

The detailed analyses of state transitions in SCLC permitted simulation of the impact of individual transitions on overall tumor composition. Our results suggest that modulating distinct state transitions in categories of tumors can markedly alter tumor composition. We also showed that tumor compositions could be experimentally modified using drugs that target the epigenome. Namely, iBET-762 and JIB-04 differentially altered Ascl1 and Yap1 states and, in turn, tumor growth rates and chemotherapy response trajectories. Although there have been previous indications of SCLC subtype differential sensitivities (*33*, *47*), the reconfiguration of SCLC cell state composition by altering state transition rates using epigenetic modifiers has not heretofore been shown. Our results also indicate that the sequencing of epigenetic therapies with chemotherapy could affect treatment efficacy. Further investigations are needed to determine the targets, dependencies on baseline state proportions, the impact of differential drug sensitivities on each state, and the most optimal sequencing with chemotherapy. Nonetheless, our results establish that SCLC state reconfiguration by certain epigenetic drug treatments is possible.

In conclusion, we have elucidated a spectrum of states of SCLC cells and their dynamics, identifying cellular programs that recapitulate neuroendocrine, neural, and mesenchymal development. Our work advances a unified dynamical model of cellular states and program diversity in SCLC and nominates therapeutic strategies designed to limit its plasticity.

MATERIALS AND METHODS

Cell culture

Cell lines from the Cancer Cell Line Encyclopedia (CCLE) were authenticated per CCLE protocol and were grown in advanced Roswell Parl Memorial Institute (RPMI) or Dulbecco's modified Eagle's medium/F12 (Thermo Fisher Scientific, MA) supplemented with 1 to 5% fetal bovine serum (FBS) (Thermo Fisher Scientific, MA), penicillin (100 U/ml), streptomycin (100 μg/ml), L-glutamine (292 μg/ml; Corning, NY), and 1% HEPES buffer solution. PDX-derived cells grown under identical media conditions were supplemented with 1% FBS. Ex vivo samples represent tumor cells derived from PDX and grown in culture for a short duration (maximum of 16 weeks). All cultures were maintained at 37°C in a humidified 5% CO_2 atmosphere and regularly tested to ensure the absence of mycoplasma. Plates were treated with 0 Gy (no radiation) or with γ-radiation delivered at 0.91 Gy/min with a ^{137}Cs source using a Gammacell 40 Exactor (Best Theratronics, ON, Canada).

Plasmids and lentiviral infections

Fluorescent reporter promoter plasmids were generated by cloning the 5′-flanking promoter sequences located ~1.5-kb upstream and up to 200–base pair downstream of the transcriptional start site (TSS) of *ASCL1*, *NEUROD1*, or *YAP1* (GeneCopoeia) upstream of reporter genes mRFP, CFP, or eGFP. The plasmids were stably integrated into ex vivo cells with a multiplicity of infection of >1, selected, and maintained in the presence of puromycin (0.01 μg/ml), hygromycin (5 μg/ml), or neomycin (25 μg/ml). Bivalent reporter–expressing cells were generated by sequential infection and selection.

Fractionation of ex vivo strata

Cellular strata of ex vivo cultures were fractionated using a four-step process: (i) Suspended cell aggregates (S^{++}) were collected by pipet transfer; (ii) the remaining strata were first suspended in Hanks' balanced salt solution (pH 7.4) (Thermo Fisher Scientific, MA) for 15 min. Semi-adherent cells (S^{+}) that entered the new suspended strata were also collected; (iii) mechanical disruption of the remaining cells facilitated the release of additional adherent cells (A^{+}); (iv) lastly, tightly adherent cells (A^{++}) were detached by enzymatic digestion using Accumax (STEMCELL Technology, Vancouver, BC). Each layer was collected into separate tubes for downstream processing.

Cellular invasion

Twenty-four–well Boyden chambers (Corning, NY) comprising semipermeable membranes with 8-μm pore size were coated with 30 to 50 μl of Matrigel (Corning, NY). A serum gradient was established by placing medium with 10% FBS in the plate well and 1% FBS in the top chamber. Established cell lines, fractionated ex vivo cells, or flow cytometry–sorted CD44- or EpCAM-expressing cells were added to the top chamber in equal cell numbers (10^5 to 10^6 cells). The plates were incubated at 37°C for 24 hours, and invasive cells were fixed and stained using 1% crystal violet solution. Invasive cells were counted using ImageJ (*48*).

Antibody and reagents

Anti-actin (CST-3700 at 1:4000 dilution), anti-Yap (CST-4912 at 1:1000 dilution), anti-NeuroD1 (CST-2833 at 1:1000 dilution), anti-Vim (CST-3932 at 1:1000 dilution), anti-CD44 (CST-5640 at 1:1000 dilution), anti-EpCAM (CST-3599 at 1:1000 dilution), anti–histone deacetylase 1 (HDAC1) (CST-5356 at 1:1000 dilution), and anti-vinculin (CST-4650 at 1:4000 dilution) were from Cell Signaling Technology (Beverly, MA). Anti-Ascl1 (sc-390794 at 1:4000 dilution) was from Santa Cruz Biotechnology (Dallas, TX). Hygromycin, neomycin, and puromycin were from MilliporeSigma (St. Louis, MO). Pharmaceutical grade cisplatin and etoposide used in murine experiments were procured from the clinical pharmacies of the affiliated hospitals.

Western blot analysis

Whole-cell lysates were prepared using M-PER lysis buffer (Thermo Fisher Scientific, MA) and clarified by centrifugation. Nuclear and cytoplasmic extractions were prepared using the NE-PER kit (Thermo Fisher Scientific, MA). Proteins were separated by SDS–polyacrylamide gel electrophoresis and transferred onto 0.45 μM nitrocellulose membranes (Maine Manufacturing, Sanford, ME). Membranes were incubated with primary antibody for 1 to 2 hours at room temperature, washed, and subsequently incubated with secondary antibodies for 1 hour. Blots were developed with an ECL chemiluminescence reagent (Amersham/GE Healthcare, Amersham, UK).

Consensus clustering and nearest centroid classification

Cell lines

Normalized RNA gene expression (Affymetrix U133 + 2 arrays) derived from 53 SCLC cell lines was downloaded from the CCLE data portal (CCLE_Expression_Entrez_2012-10-18.res at www.broadinstitute.org/ccle/home). Data were controlled for batch effects using ComBat (*49*). Expression values from the 5000 most

variable genes [as determined by median absolute deviation (MAD)] were median centered and used for downstream analyses. Consensus clustering was performed using the ConsensusClusterPlus package (*50*, *51*). 1-Pearson was used as a distance metric, resampling was set to 1000, and the maximum k was 9. The optimal number of clusters was determined by the consensus matrix and the plot of Δ area under the cummulative distribution function (CDF) curve.

Gene network classification

We created a classifier based on cluster membership and projected a gene correlation network for consensus clusters ($k = 4$) using geNetClassifier (*52*). Samples with positive silhouette widths per consensus cluster group were chosen for gene network and classifier construction.

PDX RNA-seq

Sixty-four SCLC PDXs were profiled for gene expression using RNA-seq. Reads that unambiguously aligned to the human (versus mouse) reference genome were sorted using bbsplit in BBTools (*53*). Read counts were normalized within-sample and log-transformed. The most variable genes (by MAD) were median-centered before clustering.

Correlation of cell line and PDX clusters

To determine the correspondence between cell line and PDX clusters, we created a classifier based on cluster membership using geNetClassifier (*52*). First, we calculated the silhouette widths for the samples within each cluster to find the most representative samples (*54*). Using samples with the largest silhouette widths per cluster ($n \geq 8$), we obtained the top ranked genes within each consensus cluster (posterior probability > 0.95). We then associated the cluster-specific centroids of the shared genes between the two datasets using a distance measure of 1-Pearson (*55*–*57*).

Differential gene expression

Clusters were evaluated for differentially expressed genes or gene sets using Limma (*58*). The Benjamini-Hochberg method (false discovery rate < 0.05) was used to control for multiple hypothesis testing. Gene Ontology annotations were used to determine enrichment for functional terms.

Single-cell RNA-seq

For scRNA-seq of SCLC samples, tumor aggregates were digested into single-cell suspensions as follows. Cells were treated with Accumax (STEMCELL Technology, Vancouver, BC) for 15 to 30 min in a flask using an orbital shaker at room temperature and then collected and incubated with collagenase type IV (STEMCELL Technology, Vancouver, BC) for 10 min at 37°C. The disaggregated cells were suspended in media and filtered using a 40-μm membrane (Thermo Fisher Scientific, MA) to remove undissociated aggregates. Live cells were sorted before library construction. Single cells were processed through the 10X Chromium 3′ Single Cell Platform using the Chromium Single Cell 3′ Library, Gel Bead, and Chip Kits (10X Genomics, Pleasanton, CA), following the manufacturer′s protocol. Cell Ranger version 3.0.2 was used to convert Illumina base call files to FASTQ files, which were aligned to the hg19 human reference genome and transcriptome provided by 10X Genomics. The gene versus cell count matrix was used for downstream analysis. The raw reads were processed to obtain the unique molecular identifier (UMI). Cells with fewer than 3000 expressed genes, with a high proportion of mitochondrial reads (>25%) or low proportion of ribosomal reads (<0.05%), were also removed. Genes expressed in <10% cells were also filtered out. The UMI counts were transformed and normalized using 1, with the normalization method and the scale factor set to 10,000 total UMIs per cell. Visualization was performed using SCANPY (*59*). Highly variable genes with a mean expression range of 0.0125 to 3 and a minimum dispersion of 0.5 were selected for further analyses (~2400 genes). Batch effects among the samples were adjusted using Combat within SCANPY. The Leiden algorithm was used to do identify cell clusters, and UMAP plots were used for visualization. The top 100 differentially expressed genes in each cluster (1 versus all others) were identified using the Student t test (data S4).

Flow cytometry

Single-cell suspensions were incubated with 0.05 μg of anti-CD44 (#17-0441-82, Thermo Fisher Scientific, MA), 0.05 μg of anti-EpCAM (#14-9326-95, Thermo Fisher Scientific, MA), and DAPI (R&D Systems, MN). Cells were then washed and resuspended in presort buffer (BD Biosciences, CA) for fluorescence-activated cell sorting (FACS) using the BD Biosystems Aria II flow cytometer. For FP-expressing TF reporter cells, single cells were suspended in media and sorted using 640-nm (Zombie NIR, 750LP filter), 355-nm (Calcein Blue AM, 460/50 filter), 488-nm (CD45-PerCP, 692/40 filter), and 488-nm (GFP, 530/40 filter) lasers. Side scatter width versus forward scatter (FSC) area and trigger pulse width versus FSC criteria were used to discriminate doublets and gate only single cells. We sorted viable FP-positive and FP-negative single cells into round-bottom 5-ml FACS tubes. Cells were snap-frozen immediately after sorting and stored at −80°C before whole transcriptome amplification, library preparation, and sequencing.

Clonogenicity

Ex vivo cells were FACS-sorted using anti-CD44 or anti-EpCAM at a rate of 1 cell per well in a 96-well clear, round-bottom plate (Corning, NY). Plates were incubated for ~6 weeks, and macroscopic colonies were counted manually. In vivo clonogenicity was evaluated by limiting dilution assays. Briefly, 10^2 to 10^5 cells were injected subcutaneously into NOD.Cg-*Prkdc*^{scid} *Il2rg*^{tm1Wjl}/SzJ (NSG) mice, and caliper measurements were used to monitor tumor growth for ~12 weeks.

Ex vivo imaging and single-cell tracking

Time-lapse live-cell fluorescence images were acquired using a multimode microplate reader, BioTek Cytation 1 or 5 with BioSpa 8 (Winooski, VT). Images were captured at ×4 (scale of 300 μm) or ×10 (scale of 100 μm) magnification every 1.5 or 2 hours for a duration of 100 to 200 hours. Phase contrast images were acquired using an inverted Leica ×10 to ×20 (scale of 100 and 50 μm, respectively) optical magnification microscope. Representative images of cells magnified between ×10 and ×40 were cropped to depict the individual cell types. PDX-derived ex vivo cells were dissociated in Accumax (STEMCELL Technology, Vancouver, BC) by incubation for 15 min in a flask on an orbital shaker at room temperature. Cell suspensions were then plated into 96-well clear-bottom black microplates (Corning, NY). Five micrograms of growth factor–reduced Matrigel (Corning, NY) was mixed into the medium before cell plating to reduce buoyancy, therefore limiting motion artifacts. Cell densities ranged from 1 to 2×10^4 cells per well. Cells were treated with vehicle (dimethyl sulfoxide), iBET-762, or JIB-04 (Cayman Chemical, MI). Imaging commenced 48 to 72

hours after plating. Images were processed using FIJI, an image processing package with built-in ImageJ (*48*). Single-cell tracking of fluorescent cells was implemented using a FIJI plugin, TrackMate. Cellular displacement, aspect ratios, and cluster size represented the average of four high-power fields from serial images for the duration of tracks for each sample. Each ex vivo sample was serially imaged in at least two wells per condition across two biological replicates.

DAPI staining

Ex vivo cells grown in a 96-well format were incubated with DAPI (1.0 μg/ml; BD Biosciences, NJ). Fluorescent microscopy images were obtained using the BioTek Cytation 5 fluorescent microscope system with a ×10 magnification. Images were processed using FIJI, an image processing package with built-in ImageJ (*48*). Quantification was done in quadruplicates (four wells) at two high-power fields per well, counting a minimum of 3000 total cells per high-power field.

Mouse studies

NSG mice were purchased from the Jackson Laboratory (Bar Harbor, ME, USA) and bred at the affiliated hospital facilities. All animal studies were conducted under protocols approved by the Institutional Animal Care and Use Committees. Biological material was obtained from patients who provided written informed consent under approval from the Institutional Review Board (protocol no. 07-267). Tumors were mechanically processed into submillimeter pieces in antibiotic-containing RPMI medium, combined with Matrigel (Corning, NY) and implanted into the flank of NSG mice using a syringe with a 20-gauge needle. Tumor volume was calculated using the formula (length × width^2)/2 (*60*). Tumors were harvested and stored for biological assays upon reaching a size of ≤1000 mm^3. Mice were randomized into treatment arms when tumors reached ~300 to 400 mm^3 in volume. iBET-762 (0.4 mg/kg) and JIB-04 (32 mg/kg) were formulated according to the manufacturer's specifications and administered to mice as three doses given every other day by oral gavage. Mice were treated with cisplatin and etoposide at 4:8 mg/kg ratio for 1 cycle (three doses 1 week apart). To establish whether intergroup differences were significant, we used regression with random effect and autoregressive errors (*61*, *62*).

Genetic data

RNA and DNA were isolated from PDX with the AllPrep RNA/DNA/Protein Midi Kit (QIAGEN, Hilden, Germany). RNA concentrations were quantified using NanoDrop 2000 (Thermo Fisher Scientific, MA). DNA concentrations were quantified with Qubit 4 (Thermo Fisher Scientific, MA). Total RNA was converted to mRNA libraries using the lllumina mRNA TruSeq kit, and libraries were sequenced on the Illumina HiSeq 2500. For PDX explants (not ex vivo passaged), we assessed the differential mappability of mouse reads on to the mouse and human reference genomes (*mm10* and *hg19*) using BBmap (*63*). The median of the reads that mapped to the human reference was 83.13%. Mouse and ambiguous reads were filtered out for downstream analyses. RNA reads were aligned to the *hg19* genome assembly using STAR (*64*). Exome capture of CCX1 and its strata was performed using paired-end sequencing on the Illumina HiSeq platform. Copy number alterations were estimated from exome capture data using TITAN (*65*).

Subclone reconstruction

Subclone reconstruction was performed using PhyloWGS (*41*). Briefly, up to 2500 sampled trees were calculated for each tumor using Markov chain Monte Carlo settings. Trees were ranked using a normalized log likelihood to determine the solutions that best describe the input. Sequencing error rates were assumed to be uniform across the genome.

ATAC-seq

ATAC-seq was performed as previously described (*66*). Following DNA purification, library fragments were polymerase chain reaction (PCR)–amplified with Nextera XT v2 adapter primers. Sequencing was performed on the NextSeq 500 (Illumina) from paired ends according to the manufacturer's instructions. Illumina sequencing adapter was removed from raw sequence files in FASTQ format using Cutadapt. The reads were aligned to the hg19 reference genome using Bowtie2 with -k 1 and default parameters and used after removing PCR duplicates with SAMtools and filtered off an ATAC blacklist (*66*) for mitochondrial DNA and homologous sequences. Both fragment ends were shifted +4 nucleotides (nt) for positive strand and −5 nt for negative strand to account for the distance from Tn5 binding and helicase activity to identify cut sites. HOMER was used for calling peaks with the "-style dnase" parameter. Peak files were merged, and the HOMER function "annotatePeaks.pl" was used to count the number of reads that correspond to each peak in the merged peaks. The fraction of reads in peak scores was calculated for each sample and was used as a normalization factor for pileup rescaled to a total number of uniquely alignable sequences by WigMath function of Java-Genomic Toolkit. Normalized ATAC-seq signals for each sample were visualized using Trackplot (*67*).

Clinical characteristics

Human tumor material and associated clinical data were obtained after written informed consent on an Institutional Review Board–approved prospective registry study (protocol no. 07-267). Patients with a pathological diagnosis of SCLC and a successfully engrafted PDX were selected for further evaluation. A total of 64 patients met our eligibility criteria. One patient was on erlotinib therapy and subsequently diagnosed with SCLC transformation (CBX130B). However, this patient did not receive chemotherapy before sample collection. Therefore, all samples were considered SCLC treatment naïve at the time of collection. Length of follow-up was determined from the diagnosis (biopsy) date, and patients who had not died were censored at the time of last chest imaging. Response Evaluation Criteria in Solid Tumors (RECIST) were used to evaluate the response to first-line chemotherapy ± radiation (*68*). Death without evidence of progression was treated as a competing event. Age, gender, maximum standardized uptake values (SUVmax) from positron emission tomography/computed tomography (PET/CT) scans, tumor stage, surgery, and chemotherapy use were subjected to univariate analyses. The median scores for *ASCL1*, *NEUROD1*, and *YAP1* expression (measured by TPM) were used to stratify patients into high and low expression groups. Actuarial analysis was used to estimate rates of overall survival, and the Kaplan-Meier method was used to generate overall survival curves. Cumulative incidence curves for disease progression were estimated using the competing risk method, and Gray's test was used to determine significance between cumulative incidence

curves (*69*). Statistical analysis was performed using R 3.6.2 (The R Foundation, Vienna, Austria) (*70*).

Supplementary Materials

This PDF file includes:
Supplementary Materials and Methods
Figs. S1 to S21
Table S1

Other Supplementary Material for this manuscript includes the following:
Data file S1 to S5
Movies S1 to S8

View/request a protocol for this paper from *Bio-protocol*.

REFERENCES AND NOTES

1. J. Seger, H. J. Brockmann, What is bet-hedging? *Oxford Surv. Evol. Biol.* **4**, 182–211 (1987).
2. D. Nichol, M. Robertson-Tessi, P. Jeavons, A. R. A. Anderson, Stochasticity in the genotype-phenotype map: Implications for the robustness and persistence of bet-hedging. *Genetics* **204**, 1523–1539 (2016).
3. A. S. Trigos, R. B. Pearson, A. T. Papenfuss, D. L. Goode, How the evolution of multicellularity set the stage for cancer. *Br. J. Cancer* **118**, 145–152 (2018).
4. P. B. Gupta, C. M. Fillmore, G. Jiang, S. D. Shapira, K. Tao, C. Kuperwasser, E. S. Lander, Stochastic state transitions give rise to phenotypic equilibrium in populations of cancer cells. *Cell* **146**, 633–644 (2011).
5. G. M. Süel, J. Garcia-Ojalvo, L. M. Liberman, M. B. Elowitz, An excitable gene regulatory circuit induces transient cellular differentiation. *Nature* **440**, 545–550 (2006).
6. C. J. Creighton, X. Li, M. Landis, J. Michael Dixon, V. M. Neumeister, A. Sjolund, D. L. Rimm, H. Wong, A. Rodriguez, J. I. Herschkowitz, C. Fan, X. Zhang, X. He, A. Pavlick, M. Carolina Gutierrez, L. Renshaw, A. A. Larionov, D. Faratian, S. G. Hilsenbeck, C. M. Perou, M. T. Lewis, J. M. Rosen, J. C. Chang, Residual breast cancers after conventional therapy display mesenchymal as well as tumor-initiating features. *Proc. Natl. Acad. Sci. U.S.A.* **106**, 13820–13825 (2009).
7. W. A. Woodward, M. S. Chen, F. Behbod, M. P. Alfaro, T. A. Buchholz, J. M. Rosen, WNT/beta-catenin mediates radiation resistance of mouse mammary progenitor cells. *Proc. Natl. Acad. Sci. U.S.A.* **104**, 618–623 (2007).
8. S. Bao, Q. Wu, R. E. McLendon, Y. Hao, Q. Shi, A. B. Hjelmeland, M. W. Dewhirst, D. D. Bigner, J. N. Rich, Glioma stem cells promote radioresistance by preferential activation of the DNA damage response. *Nature* **444**, 756–760 (2006).
9. A. G. Nicholson, K. Chansky, J. Crowley, R. Beyruti, K. Kubota, A. Turrisi, W. E. E. Eberhardt, J. van Meerbeeck, R. Rami-Porta; Staging and Prognostic Factors Committee Advisory Boards and Participating Institutions, The International association for the study of lung cancer lung cancer staging project: Proposals for the revision of the clinical and pathologic staging of small cell lung cancer in the forthcoming eighth edition of the TNM classification for lung cancer. *J. Thorac. Oncol.* **11**, 300–311 (2016).
10. S. Sundstrøm, R. M. Bremnes, S. Kaasa, U. Aasebø, R. Hatlevoll, R. Dahle, N. Boye, M. Wang, T. Vigander, J. Vilsvik, E. Skovlund, E. Hannisdal, S. Aamdal; Norwegian Lung Cancer Study Group, Cisplatin and etoposide regimen is superior to cyclophosphamide, epirubicin, and vincristine regimen in small-cell lung cancer: Results from a randomized phase III trial with 5 years' follow-up. *J. Clin. Oncol.* **20**, 4665–4672 (2002).
11. M. Reck, D. Rodríguez-Abreu, A. G. Robinson, R. Hui, T. Csőszi, A. Fülöp, M. Gottfried, N. Peled, A. Tafreshi, S. Cuffe, M. O. 'Brien, S. Rao, K. Hotta, M. A. Leiby, G. M. Lubiniecki, Y. Shentu, R. Rangwala, J. R. Brahmer; KEYNOTE-024 Investigators, Pembrolizumab versus chemotherapy for PD-L1-positive non-small-cell lung cancer. *N. Engl. J. Med.* **375**, 1823–1833 (2016).
12. L. Horn, A. S. Mansfield, A. Szczęsna, L. Havel, M. Krzakowski, M. J. Hochmair, F. Huemer, G. Losonczy, M. L. Johnson, M. Nishio, M. Reck, T. Mok, S. Lam, D. S. Shames, J. Liu, B. Ding, A. Lopez-Chavez, F. Kabbinavar, W. Lin, A. Sandler, S. V. Liu; IMpower133 Study Group, First-line atezolizumab plus chemotherapy in extensive-stage small-cell lung cancer. *N. Engl. J. Med.* **379**, 2220–2229 (2018).
13. L. A. Byers, C. M. Rudin, Small cell lung cancer: Where do we go from here? *Cancer* **121**, 664–672 (2015).
14. J. George, J. S. Lim, S. J. Jang, Y. Cun, L. Ozretić, G. Kong, F. Leenders, X. Lu, L. Fernández-Cuesta, G. Bosco, C. Müller, I. Dahmen, N. S. Jahchan, K.-S. Park, D. Yang, A. N. Karnezis, D. Vaka, A. Torres, M. S. Wang, J. O. Korbel, R. Menon, S.-M. Chun, D. Kim, M. Wilkerson, N. Hayes, D. Engelmann, B. Pützer, M. Bos, S. Michels, I. Vlasic, D. Seidel, B. Pinther, P. Schaub, C. Becker, J. Altmüller, J. Yokota, T. Kohno, R. Iwakawa, K. Tsuta, M. Noguchi, T. Muley, H. Hoffmann, P. A. Schnabel, I. Petersen, Y. Chen, A. Soltermann, V. Tischler, C.-M. Choi, Y.-H. Kim, P. P. Massion, Y. Zou, D. Jovanovic, M. Kontic, G. M. Wright, P. A. Russell, B. Solomon, I. Koch, M. Lindner, L. A. Muscarella, A. la Torre, J. K. Field, M. Jakopovic, J. Knezevic, E. Castaños-Vélez, L. Roz, U. Pastorino, O.-T. Brustugun, M. Lund-Iversen, E. Thunnissen, J. Köhler, M. Schuler, J. Botling, M. Sandelin, M. Sanchez-Cespedes, H. B. Salvesen, V. Achter, U. Lang, M. Bogus, P. M. Schneider, T. Zander, S. Ansén, M. Hallek, J. Wolf, M. Vingron, Y. Yatabe, W. D. Travis, P. Nürnberg, C. Reinhardt, S. Perner, L. Heukamp, R. Büttner, S. A. Haas, E. Brambilla, M. Peifer, J. Sage, R. K. Thomas, Comprehensive genomic profiles of small cell lung cancer. *Nature* **524**, 47–53 (2015).
15. M. D. Borromeo, T. K. Savage, R. K. Kollipara, M. He, A. Augustyn, J. K. Osborne, L. Girard, J. D. Minna, A. F. Gazdar, M. H. Cobb, J. E. Johnson, ASCL1 and NEUROD1 reveal heterogeneity in pulmonary neuroendocrine tumors and regulate distinct genetic programs. *Cell Rep.* **16**, 1259–1272 (2016).
16. C. M. Rudin, J. T. Poirier, L. A. Byers, C. Dive, A. Dowlati, J. George, J. V. Heymach, J. E. Johnson, J. M. Lehman, D. M. Pherson, P. P. Massion, J. D. Minna, T. G. Oliver, V. Quaranta, J. Sage, R. K. Thomas, C. R. Vakoc, A. F. Gazdar, Molecular subtypes of small cell lung cancer: A synthesis of human and mouse model data. *Nat. Rev. Cancer* **19**, 289–297 (2019).
17. M. Borges, R. I. Linnoila, H. J. van de Velde, H. Chen, B. D. Nelkin, M. Mabry, S. B. Baylin, D. W. Ball, An achaete-scute homologue essential for neuroendocrine differentiation in the lung. *Nature* **386**, 852–855 (1997).
18. E. R. Neptune, M. Podowski, C. Calvi, J.-H. Cho, J. G. N. Garcia, R. Tuder, R. Ilona Linnoila, M.-J. Tsai, H. C. Dietz, Targeted disruption of NeuroD, a proneural basic helix-loop-helix factor, impairs distal lung formation and neuroendocrine morphology in the neonatal lung. *J. Biol. Chem.* **283**, 21160–21169 (2008).
19. K. McColl, G. Wildey, N. Sakre, M. B. Lipka, M. Behtaj, A. Kresak, Y. Chen, M. Yang, V. Velcheti, P. Fu, A. Dowlati, Reciprocal expression of INSM1 and YAP1 defines subgroups in small cell lung cancer. *Oncotarget* **8**, 73745–73756 (2017).
20. J. T. Poirier, E. E. Gardner, N. Connis, A. L. Moreira, E. de Stanchina, C. L. Hann, C. M. Rudin, DNA methylation in small cell lung cancer defines distinct disease subtypes and correlates with high expression of EZH2. *Oncogene* **34**, 5869–5878 (2015).
21. D. W. Ball, C. G. Azzoli, S. B. Baylin, D. Chi, S. Dou, H. Donis-Keller, A. Cumaraswamy, M. Borges, B. D. Nelkin, Identification of a human achaete-scute homolog highly expressed in neuroendocrine tumors. *Proc. Natl. Acad. Sci. U.S.A.* **90**, 5648–5652 (1993).
22. M. Horie, A. Saito, M. Ohshima, H. I. Suzuki, T. Nagase, YAP and TAZ modulate cell phenotype in a subset of small cell lung cancer. *Cancer Sci.* **107**, 1755–1766 (2016).
23. Y.-H. Huang, O. Klingbeil, X.-Y. He, X. S. Wu, G. Arun, B. Lu, T. D. D. Somerville, J. P. Milazzo, J. E. Wilkinson, O. E. Demerdash, D. L. Spector, M. Egeblad, J. Shi, C. R. Vakoc, POU2F3 is a master regulator of a tuft cell-like variant of small cell lung cancer. *Genes Dev.* **32**, 915–928 (2018).
24. S. Qu, P. Fetsch, A. Thomas, Y. Pommier, D. S. Schrump, M. M. Miettinen, H. Chen, Molecular subtypes of primary SCLC tumors and their associations with neuroendocrine and therapeutic markers. *J. Thorac. Oncol.* **17**, 141–153 (2021).
25. M. K. Baine, M.-S. Hsieh, W. Victoria Lai, J. V. Egger, A. A. Jungbluth, Y. Daneshbod, A. Beras, R. Spencer, J. Lopardo, F. Bodd, J. Montecalvo, J. L. Sauter, J. C. Chang, D. J. Buonocore, W. D. Travis, T. Sen, J. T. Poirier, C. M. Rudin, N. Rekhtman, SCLC subtypes defined by ASCL1, NEUROD1, POU2F3, and YAP1: A comprehensive immunohistochemical and histopathologic characterization. *J. Thorac. Oncol.* **15**, 1823–1835 (2020).
26. D. N. Carney, A. F. Gazdar, G. Bepler, J. G. Guccion, P. J. Marangos, T. W. Moody, M. H. Zweig, J. D. Minna, Establishment and identification of small cell lung cancer cell lines having classic and variant features. *Cancer Res.* **45**, 2913–2923 (1985).
27. J. Calbo, E. van Montfort, N. Proost, E. van Drunen, H. B. Beverloo, R. Meuwissen, A. Berns, A functional role for tumor cell heterogeneity in a mouse model of small cell lung cancer. *Cancer Cell* **19**, 244–256 (2011).
28. M. C. Kwon, N. Proost, K. Sutherland, J. Zevenhoven, A. Berns, Functional role for tumor heterogeneity: Paracrine signaling between tumor subclones of mouse SCLC promotes metastasis. *Cancer Res.* **75**, LB-201 (2015).
29. V. Sriuranpong, M. W. Borges, C. L. Strock, E. K. Nakakura, D. Neil Watkins, C. M. Blaumueller, B. D. Nelkin, D. W. Ball, Notch signaling induces rapid degradation of achaete-scute homolog 1. *Mol. Cell. Biol.* **22**, 3129–3139 (2002).
30. H. Chen, A. Thiagalingam, H. Chopra, M. W. Borges, J. N. Feder, B. D. Nelkin, S. B. Baylin, D. W. Ball, Conservation of the Drosophila lateral inhibition pathway in human lung cancer: A hairy-related protein (HES-1) directly represses achaete-scute homolog-1 expression. *Proc. Natl. Acad. Sci. U.S.A.* **94**, 5355–5360 (1997).
31. J. S. Lim, A. Ibaseta, M. M. Fischer, B. Cancilla, G. O. 'Young, S. Cristea, V. C. Luca, D. Yang, N. S. Jahchan, C. Hamard, M. Antoine, M. Wislez, C. Kong, J. Cain, Y.-W. Liu, A. M. Kapoun, K. C. Garcia, T. Hoey, C. L. Murriel, J. Sage, Intratumoural heterogeneity generated by Notch signalling promotes small-cell lung cancer. *Nature* **545**, 360–364 (2017).

32. A. S. Ireland, A. M. Micinski, D. W. Kastner, B. Guo, S. J. Wait, K. B. Spainhower, C. C. Conley, O. S. Chen, M. R. Guthrie, D. Soltero, Y. Qiao, X. Huang, S. Tarapcsák, S. Devarakonda, M. D. Chalishazar, J. Gertz, J. C. Moser, G. Marth, S. Puri, B. L. Witt, B. T. Spike, T. G. Oliver, MYC drives temporal evolution of small cell lung cancer subtypes by reprogramming neuroendocrine fate. *Cancer Cell* **38**, 60–78.e12 (2020).
33. G. Mollaoglu, M. R. Guthrie, S. Böhm, J. Brägelmann, I. Can, P. M. Ballieu, A. Marx, J. George, C. Heinen, M. D. Chalishazar, H. Cheng, A. S. Ireland, K. E. Denning, A. Mukhopadhyay, J. M. Vahrenkamp, K. C. Berrett, T. L. Mosbruger, J. Wang, J. L. Kohan, M. E. Salama, B. L. Witt, M. Peifer, R. K. Thomas, J. Gertz, J. E. Johnson, A. F. Gazdar, R. J. Wechsler-Reya, M. L. Sos, T. G. Oliver, MYC drives progression of small cell lung cancer to a variant neuroendocrine subtype with vulnerability to aurora kinase inhibition. *Cancer Cell* **31**, 270–285 (2017).
34. C. A. Stewart, C. M. Gay, Y. Xi, S. Sivajothi, V. Sivakamasundari, J. Fujimoto, M. Bolisetty, P. M. Hartsfield, V. Balasubramaniyan, M. D. Chalishazar, C. Moran, N. Kalhor, J. Stewart, H. Tran, S. G. Swisher, J. A. Roth, J. Zhang, J. de Groot, B. Glisson, T. G. Oliver, J. V. Heymach, I. Wistuba, P. Robson, J. Wang, L. A. Byers, Single-cell analyses reveal increased intratumoral heterogeneity after the onset of therapy resistance in small-cell lung cancer. *Nat. Cancer* **1**, 423–436 (2020).
35. C. M. Gay, C. Allison Stewart, E. M. Park, L. Diao, S. M. Groves, S. Heeke, B. Y. Nabet, J. Fujimoto, L. M. Solis, W. Lu, Y. Xi, R. J. Cardnell, Q. Wang, G. Fabbri, K. R. Cargill, N. I. Vokes, K. Ramkumar, B. Zhang, C. M. Della Corte, P. Robson, S. G. Swisher, J. A. Roth, B. S. Glisson, D. S. Shames, I. I. Wistuba, J. Wang, V. Quaranta, J. Minna, J. V. Heymach, L. A. Byers, Patterns of transcription factor programs and immune pathway activation define four major subtypes of SCLC with distinct therapeutic vulnerabilities. *Cancer Cell* **39**, 346–360.e7 (2021).
36. A. R. Udyavar, D. J. Wooten, M. Hoeksema, M. Bansal, A. Califano, L. Estrada, S. Schnell, J. M. Irish, P. P. Massion, V. Quaranta, Novel hybrid phenotype revealed in small cell lung cancer by a transcription factor network model that can explain tumor heterogeneity. *Cancer Res.* **77**, 1063–1074 (2017).
37. D. J. Wooten, S. M. Groves, D. R. Tyson, Q. Liu, J. S. Lim, R. Albert, C. F. Lopez, J. Sage, V. Quaranta, Systems-level network modeling of small cell lung cancer subtypes identifies master regulators and destabilizers. *PLOS Comput. Biol.* **15**, e1007343 (2019).
38. C. Neftel, J. Laffy, M. G. Filbin, T. Hara, M. E. Shore, G. J. Rahme, A. R. Richman, D. Silverbush, M. L. Shaw, C. M. Hebert, J. Dewitt, S. Gritsch, E. M. Perez, L. N. G. Castro, X. Lan, N. Druck, C. Rodman, D. Dionne, A. Kaplan, M. S. Bertalan, J. Small, K. Pelton, S. Becker, D. Bonal, Q.-D. Nguyen, R. L. Servis, J. M. Fung, R. Mylvaganam, L. Mayr, J. Gojo, C. Haberler, R. Geyeregger, T. Czech, I. Slavc, B. V. Nahed, W. T. Curry, B. S. Carter, H. Wakimoto, P. K. Brastianos, T. T. Batchelor, A. Stemmer-Rachamimov, M. Martinez-Lage, M. P. Frosch, I. Stamenkovic, N. Riggi, E. Rheinbay, M. Monje, O. Rozenblatt-Rosen, D. P. Cahill, A. P. Patel, T. Hunter, I. M. Verma, K. L. Ligon, D. N. Louis, A. Regev, B. E. Bernstein, I. Tirosh, M. L. Suvà, An integrative model of cellular states, plasticity, and genetics for glioblastoma. *Cell* **178**, 835–849.e21 (2019).
39. J. M. Chan, Á. Quintanal-Villalonga, V. R. Gao, Y. Xie, V. Allaj, O. Chaudhary, I. Masilionis, J. Egger, A. Chow, T. Walle, M. Mattar, D. V. K. Yarlagadda, J. L. Wang, F. Uddin, M. Offin, M. Ciampricotti, B. Qeriqi, A. Bahr, E. de Stanchina, U. K. Bhanot, W. Victoria Lai, M. J. Bott, D. R. Jones, A. Ruiz, M. K. Baine, Y. Li, N. Rekhtman, J. T. Poirier, T. Nawy, T. Sen, L. Mazutis, T. J. Hollmann, D. Pe'er, C. M. Rudin, Signatures of plasticity, metastasis, and immunosuppression in an atlas of human small cell lung cancer. *Cancer Cell* **39**, 1479–1496.e18 (2021).
40. N. S. Jahchan, J. S. Lim, B. Bola, K. Morris, G. Seitz, K. Q. Tran, L. Xu, F. Trapani, C. J. Morrow, S. Cristea, G. L. Coles, D. Yang, D. Vaka, M. S. Kareta, J. George, P. K. Mazur, T. Nguyen, W. C. Anderson, S. J. Dylla, F. Blackhall, M. Peifer, C. Dive, J. Sage, Identification and targeting of long-term tumor-propagating cells in small cell lung cancer. *Cell Rep.* **16**, 644–656 (2016).
41. A. G. Deshwar, S. Vembu, C. K. Yung, G. H. Jang, L. Stein, Q. Morris, PhyloWGS: Reconstructing subclonal composition and evolution from whole-genome sequencing of tumors. *Genome Biol.* **16**, 35 (2015).
42. T. Buder, A. Deutsch, M. Seifert, A. Voss-Böhme, CellTrans: An R package to quantify stochastic cell state transitions. *Bioinform. Biol. Insights* **11**, 1177932217712241 (2017).
43. T. Jiang, B. J. Collins, N. Jin, D. N. Watkins, M. V. Brock, W. Matsui, B. D. Nelkin, D. W. Ball, Achaete-scute complex homologue 1 regulates tumor-initiating capacity in human small cell lung cancer. *Cancer Res.* **69**, 845–854 (2009).
44. G. M. Süel, R. P. Kulkarni, J. Dworkin, J. Garcia-Ojalvo, M. B. Elowitz, Tunability and noise dependence in differentiation dynamics. *Science* **315**, 1716–1719 (2007).
45. W. A. Flavahan, E. Gaskell, B. E. Bernstein, Epigenetic plasticity and the hallmarks of cancer. *Science* **357**, eaal2380 (2017).
46. D. Yang, S. K. Denny, P. G. Greenside, A. C. Chaikovsky, J. J. Brady, Y. Ouadah, J. M. Granja, N. S. Jahchan, J. S. Lim, S. Kwok, C. S. Kong, A. S. Berghoff, A. Schmitt, H. Christian Reinhardt, K.-S. Park, M. Preusser, A. Kundaje, W. J. Greenleaf, J. Sage, M. M. Winslow, Intertumoral heterogeneity in SCLC is influenced by the cell type of origin. *Cancer Discov.* **8**, 1316–1331 (2018).
47. C. M. Bebber, E. S. Thomas, J. Stroh, Z. Chen, A. Androulidaki, A. Schmitt, M. N. Höhne, L. Stüker, C. de Pádua Alves, A. Khonsari, M. A. Dammert, F. Parmaksiz, H. L. Tumbrink, F. Beleggia, M. L. Sos, J. Riemer, J. George, S. Brodesser, R. K. Thomas, H. C. Reinhardt, S. von Karstedt, Ferroptosis response segregates small cell lung cancer (SCLC) neuroendocrine subtypes. *Nat. Commun.* **12**, 2048 (2021).
48. J. Schindelin, I. Arganda-Carreras, E. Frise, V. Kaynig, M. Longair, T. Pietzsch, S. Preibisch, C. Rueden, S. Saalfeld, B. Schmid, J.-Y. Tinevez, D. J. White, V. Hartenstein, K. Eliceiri, P. Tomancak, A. Cardona, Fiji: An open-source platform for biological-image analysis. *Nat. Methods* **9**, 676–682 (2012).
49. W. E. Johnson, C. Li, A. Rabinovic, Adjusting batch effects in microarray expression data using empirical Bayes methods. *Biostatistics* **8**, 118–127 (2007).
50. S. Monti, P. Tamayo, J. Mesirov, T. Golub, Consensus clustering: A resampling-based method for class discovery and visualization of gene expression microarray data. *Mach. Learn.* **52**, 91–118 (2003).
51. M. D. Wilkerson, D. N. Hayes, ConsensusClusterPlus: A class discovery tool with confidence assessments and item tracking. *Bioinformatics* **26**, 1572–1573 (2010).
52. S. Aibar, C. Fontanillo, C. Droste, B. Roson-Burgo, F. J. Campos-Laborie, J. M. Hernandez-Rivas, J. De Las Rivas, Analyse multiple disease subtypes and build associated gene networks using genome-wide expression profiles. *BMC Genomics* **16**Suppl 5, S3 (2015).
53. B. Bushnell, sourceforge.net/projects/bbmap/.
54. L. Lovmar, A. Ahlford, M. Jonsson, A.-C. Syvänen, Silhouette scores for assessment of SNP genotype clusters. *BMC Genomics* **6**, 35 (2005).
55. Z. Hu, C. Fan, D. S. Oh, J. S. Marron, X. He, B. F. Qaqish, C. Livasy, L. A. Carey, E. Reynolds, L. Dressler, A. Nobel, J. Parker, M. G. Ewend, L. R. Sawyer, J. Wu, Y. Liu, R. Nanda, M. Tretiakova, A. R. Orrico, D. Dreher, J. P. Palazzo, L. Perreard, E. Nelson, M. Mone, H. Hansen, M. Mullins, J. F. Quackenbush, M. J. Ellis, O. I. Olopade, P. S. Bernard, C. M. Perou, The molecular portraits of breast tumors are conserved across microarray platforms. *BMC Genomics* **7**, 96 (2006).
56. M. D. Wilkerson, X. Yin, K. A. Hoadley, Y. Liu, M. C. Hayward, C. R. Cabanski, K. Muldrew, C. R. Miller, S. H. Randell, M. A. Socinski, A. M. Parsons, W. K. Funkhouser, C. B. Lee, P. J. Roberts, L. Thorne, P. S. Bernard, C. M. Perou, D. N. Hayes, Lung squamous cell carcinoma mRNA expression subtypes are reproducible, clinically important, and correspond to normal cell types. *Clin. Cancer Res.* **16**, 4864–4875 (2010).
57. V. Walter, X. Yin, M. D. Wilkerson, C. R. Cabanski, N. Zhao, Y. du, M. K. Ang, M. C. Hayward, A. H. Salazar, K. A. Hoadley, K. Fritchie, C. G. Sailey, M. C. Weissler, W. W. Shockley, A. M. Zanation, T. Hackman, L. B. Thorne, W. D. Funkhouser, K. L. Muldrew, A. F. Olshan, S. H. Randell, F. A. Wright, C. G. Shores, D. N. Hayes, Molecular subtypes in head and neck cancer exhibit distinct patterns of chromosomal gain and loss of canonical cancer genes. *PLOS ONE* **8**, e56823 (2013).
58. M. K. Kerr, Linear models for microarray data analysis: Hidden similarities and differences. *J. Comput. Biol.* **10**, 891–901 (2003).
59. F. A. Wolf, P. Angerer, F. J. Theis, SCANPY: Large-scale single-cell gene expression data analysis. *Genome Biol.* **19**, 15 (2018).
60. M. M. Tomayko, C. P. Reynolds, Determination of subcutaneous tumor size in athymic (Nude) mice. *Cancer Chemoth. Pharm.* **24**, 148–154 (1989).
61. P. Gopal, E. I. Sarihan, E. K. Chie, G. Kuzmishin, S. Doken, N. A. Pennell, D. P. Raymond, S. C. Murthy, U. Ahmad, S. Raja, F. Almeida, S. Sethi, T. R. Gildea, C. D. Peacock, D. J. Adams, M. E. Abazeed, Clonal selection confers distinct evolutionary trajectories in BRAF-driven cancers. *Nat. Commun.* **10**, 5143 (2019).
62. R. Vargas, P. Gopal, G. B. Kuzmishin, R. De Bernardo, S. A. Koyfman, B. K. Jha, O. Y. Mian, J. Scott, D. J. Adams, C. D. Peacock, M. E. Abazeed, Case study: Patient-derived clear cell adenocarcinoma xenograft model longitudinally predicts treatment response. *Npj Precis. Oncol.* **2**, 14 (2018).
63. *BBmap*, https://github.com/BioInfoTools/BBMap (accessed 21 Mar 2019).
64. A. Dobin, C. A. Davis, F. Schlesinger, J. Drenkow, C. Zaleski, S. Jha, P. Batut, M. Chaisson, T. R. Gingeras, STAR: Ultrafast universal RNA-seq aligner. *Bioinformatics* **29**, 15–21 (2013).
65. G. Ha, A. Roth, J. Khattra, J. Ho, D. Yap, L. M. Prentice, N. Melnyk, A. McPherson, A. Bashashati, E. Laks, J. Biele, J. Ding, A. Ie, J. Rosner, K. Shumansky, M. A. Marra, C. B. Gilks, D. G. Huntsman, J. N. McAlpine, S. Aparicio, S. P. Shah, TITAN: Inference of copy number architectures in clonal cell populations from tumor whole-genome sequence data. *Genome Res.* **24**, 1881–1893 (2014).
66. J. D. Buenrostro, P. G. Giresi, L. C. Zaba, H. Y. Chang, W. J. Greenleaf, Transposition of native chromatin for fast and sensitive epigenomic profiling of open chromatin, DNA-binding proteins and nucleosome position. *Nat. Methods* **10**, 1213–1218 (2013).
67. A. Pohl, M. Beato, bwtool: A tool for bigWig files. *Bioinformatics* **30**, 1618–1619 (2014).
68. L. H. Schwartz, S. Litière, E. de Vries, R. Ford, S. Gwyther, S. Mandrekar, L. Shankar, J. Bogaerts, A. Chen, J. Dancey, W. Hayes, F. S. Hodi, O. S. Hoekstra, E. P. Huang, N. Lin, Y. Liu, P. Therasse, J. D. Wolchok, L. Seymour, RECIST 1.1-Update and clarification: From the RECIST committee. *Eur. J. Cancer* **62**, 132–137 (2016).

69. L. Scrucca, A. Santucci, F. Aversa, Regression modeling of competing risk using R: An in depth guide for clinicians. *Bone Marrow Transplant.* **45**, 1388–1395 (2010).
70. Team R. *R: A Language and Environment for Statistical Computing*. (R Foundation for Statistical Computing, 2013).

Acknowledgments: We thank D. N. Watkins for helpful discussions. We also thank the VeloSano Cancer Research Fund (ID: 958768890401) for a pilot award from 2016 to 2017, E. I. Sarihan for annotating clinical outcomes for some of the PDX-associated cases, and Northwestern University NUSeq Core for contributing to NGS-based data. **Funding:** M.E.A. was supported by National Institutes of Health R37 CA222294, National Institutes of Health P30 CA060553, National Institutes of Health U01 CA268052, and American Lung Association LCD-565365. **Author contributions:** P.G. conceived, conducted, analyzed, and interpreted some of the experimental work and contributed to the writing of the manuscript. P.G., K.R., and R.B. assisted with the computational work. A.P. and T.B. provided experimental support. C.D.P. conceived and conducted some of the experimental work and assisted with analysis and interpretation. M.E.A. conceived, analyzed, interpreted, and supervised the experimental and computational work. M.E.A. wrote the manuscript. **Competing interests:** M.E.A. has provided educational programs to the American Society of Clinical Pathology (ASCP), is an advisor to Mirati Therapeutics Inc., and receives software support from Siemens Healthineers. The other authors declare that they have no competing interests. **Data and materials availability:** Genomic data pertaining to cancer cell lines were downloaded from the CCLE (www.broadinstitute.org/ccle). Human and PDX data is deposited in https://www.ncbi.nlm.nih.gov/gap/ (dbGaP study accession: phs003102.v1.p1) per NIH and institutional guidance. Other datasets analyzed during the current study are available within the article and the Supplementary Materials. All source code has been compiled and deposited: https://zenodo.org/record/7178712#.Y083QVLMKko

Submitted 2 March 2022
Accepted 26 October 2022
Published 14 December 2022
10.1126/sciadv.abp8674